Estonian Journal of Earth Sciences
2026, **75**, 2, 83–102

https://doi.org/10.3176/earth.2026.06

www.eap.ee/earthsciences
Estonian Academy Publishers

RESEARCH ARTICLE

Received 28 October 2025
Accepted 30 April 2026
Available online 6 September 2026

Keywords:
igneous petrology, Märjamaa–Kloostri rapakivi granites, tripartite magmatic evolution, major-element geochemistry, fractional crystallization, iron redox systematics

Corresponding author:
Juan David Solano-Acosta
jusola@ttu.ee

Citation:
Solano-Acosta, J. D., Soesoo, A. and Hints, R. 2026. An updated review of major-element geochemistry, redox systematics, and petrogenesis of the Märjamaa and Kloostri rapakivi granites, Estonia. *Estonian Journal of Earth Sciences*, **75**(2), 83–102. https://doi.org/10.3176/earth.2026.06

© 2026 Authors. This is an open access article distributed under the terms and conditions of the Creative Commons Attribution (CC BY) license (http://creativecommons.org/licenses/by/4.0).

An updated review of major-element geochemistry, redox systematics, and petrogenesis of the Märjamaa and Kloostri rapakivi granites, Estonia

Juan David Solano-Acosta[a], Alvar Soesoo[a,b,c] and Rutt Hints[a]

[a] Department of Geology, Tallinn University of Technology, Ehitajate tee 5, 19086 Tallinn, Estonia

[b] Geological Survey of Estonia, F. R. Kreutzwaldi 5, 44314 Rakvere, Estonia

[c] Department of Geology, University of Tartu, Ravila 14a, 50411 Tartu, Estonia

ABSTRACT

The ~1.62 Ga Märjamaa and Kloostri rapakivi intrusions of western Estonia record a tripartite magmatic evolution during the late stages of the Wiborg rapakivi suite, emplaced in a transtensional pull-apart setting related to shear-zone reactivation during Nuna breakup and constructed through piston cauldron-subsidence processes. Whole-rock major-element geochemistry, complemented by CIPW normative phase relations, is used to constrain melt evolution, redox conditions, and crystallization patterns across three magmatic phases. Phase I formed as a deeply rooted intrusion that evolved into a piston cauldron structure through roof collapse and block assimilation, and comprises ferroan granodioritic to quartz-monzonitic compositions with lower silica and alkalis and elevated Ca and Fe–Ti–P-bearing components, reflecting relatively less evolved melts. Phase II intruded as a concentric granite ring during continued subsidence and represents the most fractionated stage, characterized by higher silica and alkalis, pronounced Ca depletion, and minimal normative Fe–Ti oxides and apatite. Phase III corresponds to the late Kloostri body emplaced by asymmetric subsidence and represents a Na-rich leucogranitic melt with the highest silica contents and the lowest abundances of Ca-bearing, Fe–Ti-bearing, and P-bearing components. Progressive differentiation from Phase I to Phase III is reflected by systematic Fe-Mg trends, whereas redox conditions are more robustly constrained by iron speciation, indicating reduced conditions in Phase II, intermediate values in Phase I, and more oxidized conditions in Phase III. Decreasing normative Fe–Ti oxides from Phase I to Phase III primarily reflect progressive differentiation rather than solely oxygen-fugacity variations, emphasizing the semi-quantitative nature of redox constraints derived from major-element data. Theoretical thermobarometric estimates indicate mid-crustal crystallization at ~3–5 kbar with progressive cooling from Phase I to Phase III.

1. Introduction

A-type granites are anhydrous felsic rocks enriched in alkaline metals and high-field strength elements (HFSE), typically emplaced in post- to anorogenic settings such as continental interiors or rift zones (Loiselle and Wones 1979; Eby 1992; Frost et al. 2001; Vigneresse 2005; Dall'Agnol and de Oliveira 2007). A-type granites typically have high incompatible element contents, including heavy rare earth elements, Zr, Nb, and Ta, but low Co, Sc, Cr, Ni, Ba, Sr, and Eu contents (Frost and Frost 1997).

Rapakivi granites, a distinctive A-type subtype, are characterized by ovoid alkali-feldspar megacrysts mantled by oligoclase (Haapala and Rämö 1992; Rämö and Haapala 1995, 2005). In the Fennoscandian province, rapakivi granites are typically subsolvus monzogranites to syenogranites, whereas rapakivi-type granitoids globally may span a broader compositional range, from quartz syenitic to locally peralkaline varieties (Vigneresse 2005; Bonin 2007; Dall'Agnol et al. 2012). These granites are widely reported from Precambrian cratons, including Baltica (East European Craton), Laurentia, and Amazonia (Puura and Flodén 1996, 1999, 2000; Bogdanova et al. 2006, 2015; Sharkov 2010; Salminen et al. 2021; Grabarczyk et al. 2023; Hinchey et al. 2024). Rapakivi-like granitoids have also been described from Phanerozoic belts, although their classification and genetic equivalence remain debated (Rajesh 2000; Christiansen et al. 2007; Luo et al. 2024).

In Fennoscandia (Fig. 1a), rapakivi granites represent Paleoproterozoic to early Mesoproterozoic anorthosite–mangerite–charnockite–granite (AMCG) magmatism, which was mainly emplaced between ~1.7–1.5 Ga, with a peak at ~1.6 Ga during

the assembly of Nuna, Columbia (Salminen et al. 2021; Johansson et al. 2022). Although AMCG magmatism persists globally until ~1.0 Ga, such younger events are absent in the Fennoscandian domain (Emslie 1978; Frost et al. 1999; Vigneresse 2005; Christiansen et al. 2007; Hinchey et al. 2024). These bimodal associations commonly include rapakivi granites, massif-type anorthosites, gabbros, ferrodioritic dikes, and mangerites (Haapala and Rämö 1992; Rämö and Haapala 1995, 2005; Dall'Agnol and de Oliveira 2007). Petrogenetic models attribute their formation to partial melting of crustal sources triggered by mantle upwelling and mafic underplating, with tectonic settings ranging from post-orogenic extension to mantle-superswell-related and thermal perturbations (Bonin 2007; Kukkonen and Lauri 2009; Sharkov 2010; Salminen et al. 2021; Johansson 2023).

In Estonia, the AMCG suite comprises smaller ~1.6 Ga granitoids, including Märjamaa (with its Kloostri satellite), Naissaare, Taebla, Neeme, and Ereda, and the ~1.5 Ga Riga batholith (Fig. 1b; Soesoo and Niin 1992; Klein et al. 1994; Rämö et al. 1996; Kirs et al. 2004). These granitoids are pink, medium- to coarse-grained syeno- to monzogranites with porphyritic textures, in which the classic plagioclase-mantled alkali-feldspar ovoids are scarce (Soesoo and Niin 1992; Klein et al. 1994). Despite their small size and the absence of associated anorthosites, they are geochemically and isotopically consistent with the Fennoscandian rapakivi suites (Klein et al. 1994; Rämö et al. 1996; Ahl et al. 1997; Kirs et al. 2004).

The Märjamaa–Kloostri intrusions were emplaced within a Svecofennian-inherited crustal framework, where deep-seated shear zones provided pathways for Paleoproterozoic

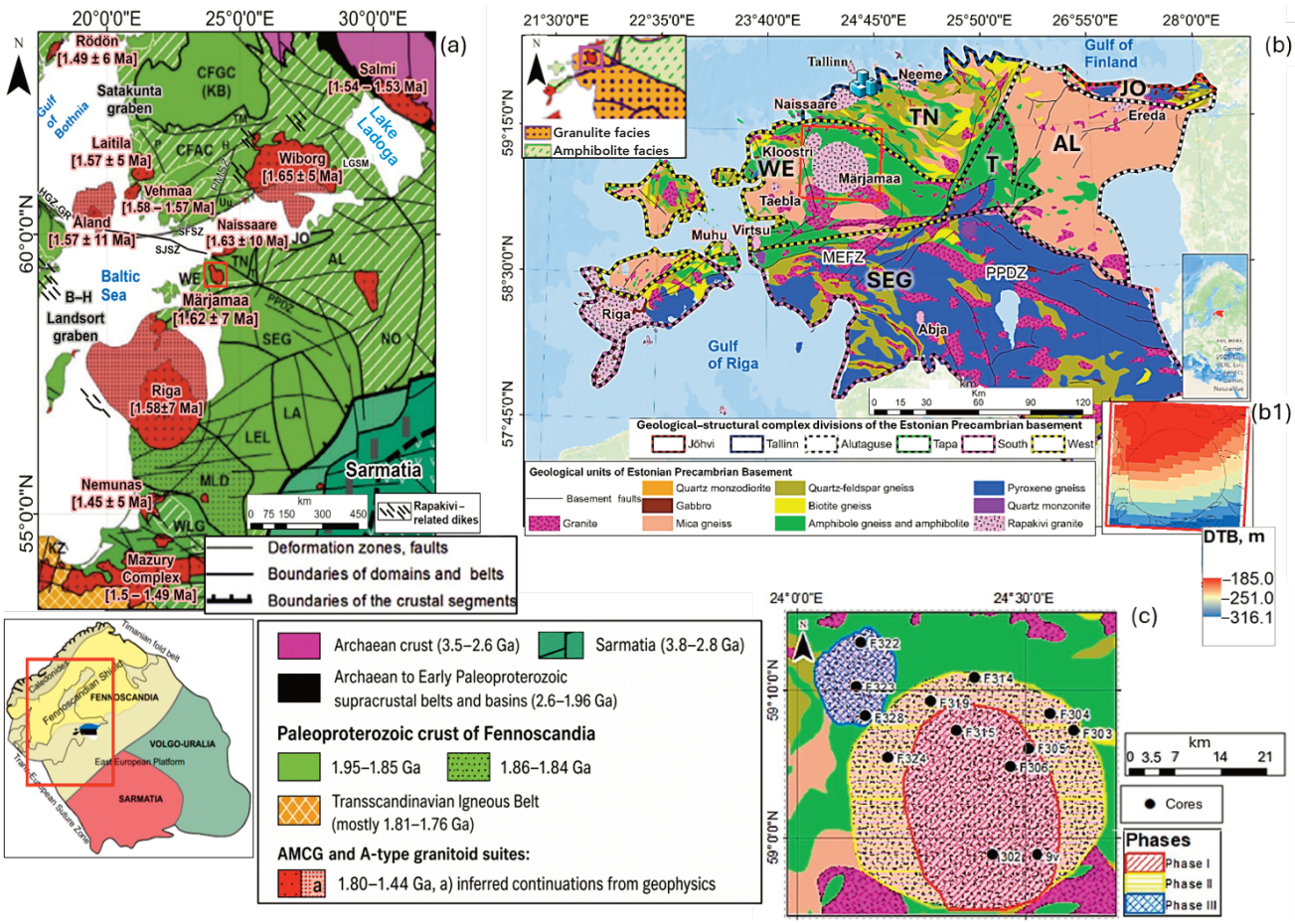

Fig. 1. Geological setting of the study zone. **(a)** Major Paleoproterozoic tectonic domains of Fennoscandia, modified after Bogdanova et al. (2015), highlighting the most prominent rapakivi bodies, with the Märjamaa and Kloostri granitoids study area marked by a red rectangle. The white diagonal ruling over the greenish area indicates Svecofennian sedimentary basins. The ages of the rapakivi granitoids of Fennoscandia are constrained from Laitakari et al. (1996), Rämö et al. (1996), Ahl et al. (1997), Skridlaitė et al. (2007), Larin (2009), Sharkov (2010), Johansson et al. (2016), and Grabarczyk et al. (2023). **(b)** Precambrian geological map highlighting the Estonian basement. The upper-left-corner inset shows the distribution of granulite- and amphibolite-facies metamorphic rocks after Bogdanova et al. (2015). Geological data are available from the Geoportal of the Republic of Estonia Land and Spatial Development Board,[1] including (b1) depth-to-basement (DTB) measurements from the same source. **(c)** Locations of drill-core samples from the dataset used by Kivisilla et al. (1999), showing the distribution of the drill-core samples superimposed on the tripartite phase-distribution map of the Märjamaa pluton and its Kloostri satellite intrusion (after Klein et al. 1994). Abbreviations: AL – Alutaguse, B–H – Breven–Hällefors dike swarms, CFAC – Central Finland Arc Complex, CFGC – Central Finland Granitoid Complex, H – Häme belt, HGZ–GR – Hagsta–Gävle–Rättvik Zone, JO – Jõhvi, KB – Keitele microcontinent, KZ – Kaszuby, LA – Latgalia, LEL – Latvian–East Lithuanian, LGSM – Late Svecofennian Granite–Migmatite Zone, MLD – Mid-Lithuanian domain, NO – Novgorod, P – Pirkanmaa belt, SEG – South Estonian granulite domain, T – Tapa, TM – Tampere belt, TN – Tallinn, Uu – Uusimaa belt, WE – West Estonian domain, WLG – West Lithuanian granulite domain. Shear and fault zones are abbreviated as follows: MEFZ – Middle-Estonian Fault Zone, PMSZ – Porkkala–Mäntsälä Shear Zone, PPDZ – Paldiski–Pskov Deformation Zone, SFSZ – South Finland Shear Zone, SJSZ – Sottunga–Jurmo Shear Zone.

[1] https://xgis.maaamet.ee/xgis2/page/app/geoloogia400k

magmatism (e.g., the Åland–Paldiski–Pskov deformation zone (Åland–PPDZ) (Fig. 1b; Puura et al. 1997; Puura and Flodén 2000; Kirs et al. 2004; All et al. 2006; Bogdanova et al. 2015; Solano-Acosta et al. 2023, 2025b). Previous studies have outlined their petrography and isotopic signatures (Soesoo and Niin 1992; Klein et al. 1994; Kirs et al. 2004), yet an updated and systematic synthesis of elemental geochemistry and magmatic evolution remains lacking.

This study presents an updated analysis of compiled whole-rock major-element data for the Märjamaa rapakivi pluton and its Kloostri satellite intrusion (Fig. 1c). We examine the geochemical evolution of its tripartite magmatic phases, focusing on their elemental trends and redox conditions, and compare them with Fennoscandian rapakivi granites within the broader AMCG context.

2. Geological setting

2.1. Regional context

Baltica, northeast of the Trans-European Suture Zone, consists of three Archean-Proterozoic proto-cratons: Fennoscandia, Volgo-Uralia, and Sarmatia (Fig. 1a). Their amalgamation at 2.1–1.79 Ga during the Svecofennian orogeny (SO) produced a stable continental core through the accretion of island arcs and microcontinents and the 1.84–1.79 Ga Svecobaltic collision, followed by collapse and stabilization at 1.79–1.77 Ga and final amalgamation of the Livonia microcontinent with Sarmatia at ~1.70 Ga (Gorbatschev and Bogdanova 1993; Nironen 1997; Bogdanova et al. 2006, 2015; Johansson et al. 2022). Subsequent evolution in southwestern Baltica was dominated by the westward-younging 1.73–1.48 Ga Gothian orogeny along its western margin (Bogdanova et al. 2008; Nironen 2017).

AMCG suites were emplaced after the Gothian orogeny within the Svecofennian Province and the Transscandinavian Igneous Belt to the south, reflecting widespread bimodal magmatism in Baltica (Ahl et al. 1997; Vigneresse 2005; Larin 2009; Salminen et al. 2021; Grabarczyk et al. 2023). Fennoscandian rapakivi granites are commonly grouped into four main age-defined suites: the Wiborg suite (1.67–1.62 Ga), the Åland suite (1.59–1.56 Ga), the Salmi suite (1.55–1.53 Ga), and the Ragunda suite (1.53–1.47 Ga) (Rämö et al. 1996; Ahl et al. 1997; Puura and Flodén 2000; Salminen et al. 2021; Grabarczyk et al. 2023). The Märjamaa–Kloostri rapakivi intrusions investigated in this study belong to the oldest Wiborg suite. These magmatic episodes are spatially associated with fault-controlled crustal blocks and long-lived lithospheric structures (Puura and Flodén 1996; All et al. 2006; Bogdanova et al. 2015; Salminen et al. 2021; Nordbäck et al. 2024; Solano-Acosta et al. 2025b).

2.2. Estonian context

The Precambrian crystalline basement of Estonia, composed of Paleoproterozoic to Mesoproterozoic metamorphic and igneous rocks (1.9–1.5 Ga), is entirely buried beneath 100–900 m of Neoproterozoic–Devonian shallow-marine sandstones, mudstones, and carbonates that thicken southward (~0.10–0.20°) (Puura et al. 1997; Kirs et al. 2004; Soesoo et al. 2020). The basement, known from drilling and geophysical data, correlates with better-exposed terranes in southern Finland and Sweden (Puura et al. 2004; Bogdanova et al. 2015; Soesoo et al. 2020; Solano-Acosta et al. 2023, 2025a, 2025b).

Six structural-petrological zones – Tallinn, Alutaguse, Jõhvi, West-Estonian, Tapa, and South-Estonian – are distinguished by lithological, geochemical, and geophysical contrasts, bounded by major crustal-scale features such as the NW–SE PPDZ and E–W Middle-Estonian Fault Zone (MEFZ) (All et al. 2004; Bogdanova et al. 2015). The Tallinn and Alutaguse domains, correlating with the Uusimaa arc and its back-arc basin, accreted with other Svecofennian terranes during 1.92–1.87 Ga double subduction and arc-microcontinent collisions (Nironen 2017; Solano-Acosta et al. 2025a). Western and southern Estonia consist of high-grade metasedimentary and orthogneissic complexes overprinted by granulite-facies metamorphism (Fig. 1b; Soesoo et al. 2004, 2020). Regional gravity and magnetic patterns show these domains as continuations of oblique Svecofennian blocks in Finland, Sweden, and Latvia, shaped by inherited NW–SE shear zones, including the PPDZ and its Sottunga–Jurmo extension, which remain seismically active (Fig. 1c; Korhonen et al. 2002; Högdahl et al. 2009; Soosalu et al. 2022; Nordbäck et al. 2024).

Estonia's Precambrian basement comprises three principal age groups. The oldest (1.92–1.80 Ga) corresponds to the Svecofennian crust and includes northern Estonian metavolcanics (~1.92 Ga), granulitic metavolcanics in southern Estonia (~1.83–1.82 Ga), and tonalitic intrusions in the Tapa area (~1.82 Ga) (Petersell and Levchenkov 1994; Soesoo et al. 2004, 2006; Kirs et al. 2009; Bogdanova et al. 2015). Magnetite-bearing gneisses of the Jõhvi belt yield zircon U–Pb ages of ~1.87–1.79 Ga (Soesoo et al. 2020). The second group corresponds to the southern Estonian tonalites, charnockites, and orthopyroxene-garnet gneisses that crystallized between ~1.79 and 1.76 Ga, while gabbro-norite dikes yield ages of ~1.77 Ga (Soesoo et al. 2004, 2006). The third group, related to a younger magmatic episode (1.64–1.58 Ga), comprises A-type granites and rapakivi granitoids emplaced during several closely spaced events, including the Taebla granitoids (~1.65 Ga), Abja shoshonitic granite (~1.64 Ga), Neeme granitoids (~1.63 Ga), and Ereda intrusions (~1.64–1.63 Ga). Slightly younger rapakivi bodies include Märjamaa (~1.63 Ga), Naissaare (~1.62 Ga), the Virtsu quartz monzonite (~1.61 Ga), and the Riga batholith (~1.58 Ga) (Fig. 1; Kirs and Petersell 1994; Rämö et al. 1996; Soesoo and Hade 2012).

Estonian rapakivi bodies and high-K shoshonitic bodies (e.g., Virtsu, Muhu, and Abja) exhibit geochemical similarities with Finnish rapakivi granites and show comparable emplacement and structural features due to the reactivation of related shear faults (Figs 1b and S1; Soesoo 1993; Kirs and Petersell 1994; Klein et al. 1994; Kirs et al. 2004; Nordbäck et al. 2024; Solano-Acosta et al. 2025b). These porphyritic plutons are characterized by prominent microcline megacrysts and are locally cross-cut by aplitic and microsyenitic dikes (Soesoo and Niin 1992). Biotite (annitic to siderophyllitic) dominates the mafic fraction, with hornblende present in Märjamaa, Naissaare, and Neeme (Soesoo 1993).

The Märjamaa intrusion is a ~40 × 25 km composite pluton emplaced into West-Estonian Proterozoic gneisses (Fig. 1b; All et al. 2004; Kirs et al. 2004; Solano-Acosta et al. 2023). It comprises three magmatic phases (Fig. 1c): Phase I is a melanocratic granodiorite containing abundant gneiss xenoliths (up to 20 cm); Phase II is a biotite-hornblende granite forming a K-feldspar-rich ring; and Phase III is represented by the adjacent northwestern Kloostri intrusion, a sodium-rich (albite-dominated) leucogranite that exhibits a trachytoid texture characterized by the preferred orientation of feldspar laths (Soesoo and Niin 1992; Klein et al. 1994; Laitakari et al. 1996). Quartz (20–30%) occurs in two generations, both as inclusions within microcline (20–40%) and as groundmass grains. Plagioclase (20–40%) is ubiquitous, biotite (2–10%) forms anhedral clusters, hornblende is restricted to Phases I–II, and the presence of muscovite confined to Phase III may hint at increased peraluminosity or fluid-rich late stages; however, as it occurs only as a minor, late-forming phase, it does not change the overall classification of the system. Magnetite and ilmenite (3–5%) are common, with zircon, apatite, titanite, fluorite, and epidote occurring as accessory minerals in all three phases (Soesoo and Niin 1992; Puura et al. 1997).

Solano-Acosta et al. (2025b) proposed a three-stage emplacement model for the Märjamaa–Kloostri complex, involving structure-controlled magma ascent along the NW-trending Åland–PPDZ. Reactivated Paleoproterozoic (SO) shear fabrics under transpressional–transtensional stress focused Mesoproterozoic AMCG magmatism (Fig. S1), promoting pull-apart basin development and piston cauldron-subsidence. Phase I originated as a deeply rooted, steep-sided tabular granodiorite intrusion that evolved into a piston cauldron geometry through progressive roof collapse and block assimilation, generating positive magnetic and Bouguer anomalies. Phase II was emplaced as a concentric granite ring during continued subsidence and is associated with negative gravity anomalies. Phase III represents the Kloostri leucogranite emplaced by asymmetric subsidence, characterized by positive magnetic but negative Bouguer signatures. Collectively, these phases record emplacement during the terminal stage of the first Fennoscandian rapakivi AMCG magmatic episode (Wiborg suite), driven by asthenospheric upwelling and mafic underplating linked to superswell activity during Nuna breakup (Pirajno and Santosh 2015; Salminen et al. 2021).

3. Materials and methods

Geochemical studies of Estonia's Precambrian basement have traditionally relied on wet-chemistry analyses of drill-core samples to determine whole-rock major-element compositions (Kivisilla et al. 1999). The compiled dataset includes SiO_2, TiO_2, Al_2O_3, Fe_2O_3, FeO, MnO, MgO, CaO, Na_2O, K_2O, P_2O_5, S_{tot}, and loss on ignition (LOI; wt.%), and is publicly available through the Estonian Research Infrastructure portal GEOkirjandus.[2] From this compilation, 47 samples from the Märjamaa pluton and the Kloostri satellite intrusion were extracted. Major-element concentrations were normalized to 100 wt.%, and Fe_2O_{3tot} and FeO^* (total iron) were subsequently calculated. Samples were assigned to Phases I, II, and III following the established Märjamaa–Kloostri phase framework (Fig. 1c), based on field relations, petrography, and geophysical constraints (Soesoo and Niin 1992; Soesoo 1993; Klein et al. 1994; Solano-Acosta et al. 2025b). The major-element data are presented in Table 1, and the associated petrogenetic relationships are summarized in Table 2.

Normative mineral proportions were calculated using the updated CIPW (Cross, Iddings, Pirsson, and Washington) norm implemented in the Python-based webNORM application[3] (Buckle et al. 2023) (Table 2; Fig. 2). The algorithm follows Verma et al. (2003) and applies the plutonic-rock iron correction of Le Maitre (1976). Because CIPW norms represent an anhydrous, idealized mineral assemblage (Kelsey 1965), hydrous minerals present in the Märjamaa–Kloostri rapakivi granites, such as biotite and hornblende (Soesoo 1993; Klein et al. 1994), are not reproduced. Normative results are used exclusively to assess bulk compositional trends and relative proportions of quartz, feldspars, Fe–Ti oxides, and phosphate phases, rather than to define modal or mineralogical compositions. Normative phases not characteristic of rapakivi granitoids, including orthopyroxene and clinopyroxene components (enstatite–ferrosilite, clinoenstatite–clinoferrosilite, and diopside) and corundum, are excluded from interpretation (Andersson and Eklund 1994; Eklund and Shebanov 1999; Rämö and Haapala 2005).

Thermobarometric estimates derived from major-element relations and normative calculations (e.g., Yang 2017; Duan et al. 2022) were obtained and are treated as theoretical, being used solely for internal comparison and contextual evaluation against published mineral-based constraints (e.g., Klein et al. 1994), rather than as substitutes for mineral-chemical thermobarometry (Andersson and Eklund 1994; Eklund et al. 1994; Elliott 2001; Sharkov and Bogina 2006).

4. Results

4.1. Major-element trends

Major-element compositions exhibit systematic variations across the three magmatic phases of the Märjamaa–Kloostri rapakivi granites (Fig. 2a). Results are reported as average values; minimum–maximum ranges are provided where available, and values without ranges represent averages only.

SiO_2 increases with magmatic evolution, averaging 66.94 wt.% (63.51–74.39 wt.%) in Phase I, 69.93 wt.% (66.34–73.86 wt.%) in Phase II, and 71.78 wt.% (70.05–75.47 wt.%) in Phase III. Al_2O_3 remains broadly stable but shows a slight decrease, with averages of 13.61 wt.% (12.58–14.29 wt.%) in Phase I, 13.42 wt.% (11.86–15.82 wt.%) in Phase II, and 13.20 wt.% (12.23–13.93 wt.%) in Phase III.

[2] https://kirjandus.geoloogia.info/reference/21247
[3] https://webnorm.streamlit.app

Sample code	ID	Core	Depth, m	Phase	SiO_2	TiO_2	Al_2O_3	Fe_2O_3	FeO	MnO	MgO	CaO	Na_2O	K_2O	P_2O_5	S_{tot}	LOI	SUM	Fe_2O_{3tot}	FeO^*	SO_3
3023300	374	302	330	I	74.39	0.10	12.58	0.35	0.76	0.01	0.40	1.77	3.19	5.98	0.01	0.03	0.44	100.00	1.19	1.07	0.07
3023320	375	302	332	I	63.80	1.08	13.73	3.03	3.68	0.04	1.84	3.80	2.94	4.60	0.46	0.09	0.90	100.00	7.12	6.40	0.23
3023344	377	302	334.4	I	67.60	0.76	13.13	2.56	2.33	0.11	1.15	3.28	2.91	4.94	0.34	0.16	0.74	100.00	5.14	4.63	0.40
3023344	376	302	334.42	I	67.47	0.81	13.21	2.62	2.32	0.11	1.13	3.44	2.91	4.75	0.37	0.16	0.70	100.00	5.20	4.68	0.40
3023700	378	302	370	I	65.63	0.73	14.29	2.01	3.00	0.01	1.35	2.99	3.31	5.66	0.32	0.07	0.63	100.00	5.34	4.81	0.18
3024031	380	302	403.1	I	73.09	0.11	13.35	1.22	0.75	0.01	0.43	1.35	2.81	6.32	0.03	0.03	0.49	100.00	2.06	1.85	0.08
3024051	381	302	405.1	I	66.25	0.78	13.86	2.07	2.88	0.01	1.40	3.06	2.86	5.61	0.34	0.09	0.80	100.00	5.27	4.74	0.23
3024384	385	302	438.4	I	65.89	0.76	13.82	2.04	3.48	0.01	1.42	3.04	3.00	5.50	0.32	0.08	0.63	100.00	5.91	5.32	0.20
3024600	388	302	460	I	65.14	0.83	13.40	2.57	2.86	0.10	1.05	4.89	2.49	5.26	0.35	0.09	0.97	100.00	5.75	5.18	0.22
3024785	390	302	478.5	I	66.32	0.93	13.56	2.22	3.19	0.02	1.61	2.94	2.89	5.07	0.39	0.08	0.77	100.00	5.77	5.19	0.20
3024805	391	302	480.5	I	66.21	0.90	14.29	2.24	3.56	0.14	1.24	2.88	2.77	4.80	0.33	0.10	0.54	100.00	6.20	5.57	0.25
3024850	393	302	485	I	66.62	0.80	13.84	2.31	2.87	0.14	1.40	2.95	3.01	5.12	0.30	0.09	0.54	100.00	5.50	4.95	0.22
3024874	394	302	487.4	I	66.01	0.89	13.17	3.01	2.81	0.11	1.66	3.27	2.77	4.92	0.43	0.20	0.74	100.00	6.13	5.52	0.50
9v3250	125	9v	325	I	64.95	0.99	13.11	3.77	2.89	0.14	1.60	3.68	2.49	4.46	0.46	0.22	1.23	100.00	6.98	6.28	0.55
9v3270	126	9v	327	I	63.51	0.88	13.86	3.77	3.07	0.28	1.76	3.37	2.47	5.10	0.48	0.18	1.28	100.00	7.18	6.46	0.44
F3052780	1374	F305	278	I	69.95	0.37	13.31	0.84	3.13	0.09	0.67	2.19	2.59	6.29	0.12	0.09	0.35	100.00	4.32	3.88	0.23
F3063064	1376	F306	306.4	I	67.69	1.11	13.62	1.93	2.67	0.10	1.38	3.13	2.59	4.82	0.32	0.09	0.55	100.00	4.90	4.41	0.23
F3063270	1377	F306	327	I	63.99	1.09	14.13	3.76	2.75	0.13	1.37	3.72	3.14	4.75	0.49	0.09	0.60	100.00	6.81	6.13	0.23
F3063430	1378	F306	343	I	67.77	0.65	13.65	1.90	2.63	0.09	1.26	3.13	2.90	5.20	0.30	0.09	0.43	100.00	4.82	4.33	0.23
F3152675	1420	F315	267.5	I	68.24	0.88	13.36	2.04	2.74	0.10	1.35	3.18	2.61	4.44	0.27	0.12	0.66	100.00	5.09	4.58	0.30
F3152813	1421	F315	281.3	I	66.87	0.90	14.06	2.26	3.06	0.12	1.56	3.30	2.31	4.34	0.34	0.11	0.76	100.00	5.66	5.10	0.28
F3153087	1422	F315	308.7	I	65.25	0.94	14.03	2.13	3.03	0.13	1.52	3.48	3.01	5.35	0.32	0.12	0.68	100.00	5.50	4.95	0.30
F3032833	1368	F303	283.3	II	69.65	0.53	13.36	0.96	3.17	0.06	0.67	2.08	2.45	6.31	0.14	0.09	0.52	100.00	4.49	4.04	0.23
F3033190	1369	F303	319	II	67.93	0.66	13.88	1.12	3.94	0.08	0.84	2.66	2.51	5.30	0.19	0.09	0.78	100.00	5.49	4.94	0.23
F3033338	1370	F303	333.8	II	69.90	0.17	15.82	0.29	1.09	0.03	0.38	1.63	2.67	7.46	0.03	0.09	0.44	100.00	1.50	1.35	0.23
F3042790	1371	F304	279	II	70.21	0.26	13.20	0.69	2.66	0.06	0.50	1.62	2.66	7.43	0.04	0.09	0.56	100.00	3.65	3.29	0.23
F3043035	1372	F304	303.5	II	71.30	0.19	13.68	0.72	2.27	0.07	0.54	1.68	2.59	6.59	0.05	0.09	0.22	100.00	3.25	2.92	0.23
F3043288	1373	F304	328.8	II	68.06	0.25	14.27	0.95	2.80	0.08	0.50	2.08	2.79	7.70	0.06	0.09	0.36	100.00	4.06	3.66	0.22
F3142442	1411	F314	244.2	II	72.77	0.34	11.86	0.92	2.16	0.05	0.50	1.50	2.38	6.49	0.03	0.09	0.90	100.00	3.32	2.99	0.23
F3142558	1412	F314	255.8	II	73.86	0.17	13.12	0.81	1.29	0.03	0.42	1.01	2.53	6.01	0.03	0.09	0.61	100.00	2.25	2.02	0.23
F3142676	1413	F314	267.6	II	72.38	0.34	12.15	1.11	2.38	0.06	0.46	1.51	2.39	6.51	0.02	0.09	0.60	100.00	3.75	3.37	0.23
F3142906	1415	F314	290.6	II	73.44	0.22	12.96	0.73	1.29	0.03	0.46	1.01	2.56	6.33	0.03	0.09	0.84	100.00	2.17	1.95	0.23
F3192560	1438	F319	256	II	66.34	0.60	14.43	1.05	3.10	0.07	1.26	2.32	2.77	6.40	0.13	0.09	1.43	100.00	4.50	4.05	0.23
F3193090	1439	F319	309	II	70.88	0.43	12.70	0.75	2.17	0.07	0.63	2.14	2.58	7.06	0.05	0.09	0.46	100.00	3.16	2.84	0.23
F3242760	1456	F324	276	II	67.08	0.74	13.30	1.47	4.61	0.13	1.12	3.26	2.63	4.65	0.37	0.10	0.54	100.00	6.59	5.93	0.25
F3243300	1457	F324	330	II	66.38	0.52	13.81	2.54	3.17	0.11	0.54	2.66	2.82	6.28	0.19	0.09	0.89	100.00	6.06	5.45	0.23
F3243312	1458	F324	331.2	II	68.72	0.56	12.83	1.68	4.01	0.11	0.89	3.13	2.52	4.79	0.30	0.09	0.36	100.00	6.14	5.52	0.23
F3222408	1449	F322	240.8	III	70.36	0.64	12.23	2.47	1.92	0.13	0.81	2.64	3.01	4.94	0.08	0.09	0.69	100.00	4.60	4.14	0.23
F3222707	1450	F322	270.7	III	70.36	0.37	13.93	1.11	1.35	0.07	0.79	1.99	3.23	6.21	0.04	0.09	0.46	100.00	2.61	2.35	0.22
F3222760	1451	F322	276	III	75.47	0.08	12.92	0.69	0.32	0.01	0.22	1.34	4.68	3.89	0.01	0.09	0.28	100.00	1.05	0.94	0.23
F3232892	1452	F323	289.2	III	73.07	0.14	13.07	1.79	0.61	0.03	0.45	1.72	3.67	4.63	0.02	0.09	0.70	100.00	2.48	2.23	0.23
F3233042	1453	F323	304.2	III	72.68	0.25	13.31	0.79	1.19	0.04	0.53	1.72	2.81	6.02	0.03	0.09	0.54	100.00	2.12	1.91	0.23
F3233310	1454	F323	331	III	72.57	0.25	13.86	1.89	0.36	0.07	0.36	1.49	3.04	5.67	0.04	0.09	0.31	100.00	2.29	2.06	0.23
F3233330	1455	F323	333	III	71.74	0.33	13.27	0.89	1.33	0.07	0.62	1.89	3.20	6.00	0.03	0.09	0.53	100.00	2.37	2.13	0.22
F3282580	1467	F328	258	III	70.55	0.40	13.33	1.15	1.64	0.06	0.62	2.06	3.49	6.23	0.05	0.09	0.34	100.00	2.97	2.67	0.22
F3282810	1468	F328	281	III	70.05	0.44	13.37	1.36	1.54	0.07	0.58	2.32	3.40	6.26	0.05	0.09	0.46	100.00	3.07	2.77	0.22
F3283100	1469	F328	310	III	70.97	0.42	12.68	1.54	1.63	0.10	1.08	2.27	2.94	5.81	0.04	0.09	0.43	100.00	3.35	3.01	0.23

Table 1. Major-element data (wt.%) compiled from Kivisilla et al. (1999), organized by location, drill core, and magmatic phase, as illustrated in Fig. 1c. Data were normalized to 100 wt.%. Only analyses of fresh to slightly altered rocks are included, for which the sum of the original (non-normalized) major oxides lies within 100 ± 1.5 wt.% and the loss on ignition (LOI) of silicate rocks is < 3 wt.%, indicating acceptable analytical precision and limited alteration. Total iron was recalculated as $Fe_2O_{3tot} = Fe_2O_3 + 1.111\ FeO$, with total ferrous iron expressed as $FeO^* = 0.8998\ Fe_2O_{3tot}$. Sulfur contents were converted to sulfate as SO_3 [wt.%] = S [wt.%] × (80.07/32.07)

Table 2. Presented in two parts. Continued on the next page

Sample code	Geochemical relations																		
	DF1	DF2	K_2O/Na_2O	FeO^*/MgO	Mg#	A/NK	ASI	$Na_2O + K_2O$	$FeO^*/(FeO^* + MgO)$	Fe#	Fe_2O_3/FeO	X_{Mag}	MALI	T_{SiO}, °C$_2$	T_{MgO}, °C	P_{Qtz}, MPa	P_{Ab-Or}, MPa	P_{Qtz}, kbar	P_{Ab-Or}, kbar
3023300	–2.47	–1.11	1.79	3.92	31.26	1.47	0.84	6.95	0.80	1.30	0.68	0.84	3.27	803.26	929.96	212.17	225.41	2.12	2.25
3023320	–2.65	–0.73	2.06	3.67	32.71	1.45	0.88	7.57	0.79	1.23	0.71	0.88	4.21	823.67	938.75	470.59	485.99	4.71	4.86
3023344	–1.87	–1.00	1.88	2.69	39.89	1.07	0.84	9.17	0.73	0.46	0.81	0.84	7.39	669.67	810.43	244.05	257.71	2.44	2.58
3023344	–1.46	–1.57	1.56	3.48	33.85	1.40	0.82	7.54	0.78	0.83	0.67	0.82	3.75	819.58	942.68	547.40	563.17	5.47	5.63
3023700	–2.30	–1.10	1.63	4.13	30.13	1.33	0.82	7.66	0.81	1.13	0.67	0.82	4.22	767.55	898.52	262.09	275.95	2.62	2.76
3024031	–2.35	–1.06	1.70	4.03	30.67	1.30	0.82	7.85	0.80	1.10	0.68	0.82	4.56	765.78	899.84	292.12	306.28	2.92	3.06
3024051	–1.45	–2.66	1.71	3.55	33.41	1.24	0.84	8.97	0.78	0.67	0.71	0.84	5.98	793.75	914.54	1144.55	1162.03	11.45	11.62
3024384	–4.17	–3.46	2.25	4.30	29.33	1.17	0.96	9.12	0.81	1.63	0.87	0.96	7.77	688.03	816.73	249.01	262.73	2.49	2.63
3024600	–1.65	–2.69	1.96	3.38	34.53	1.29	0.85	8.47	0.77	0.72	0.69	0.85	5.41	784.95	917.81	598.99	614.97	5.99	6.15
3024785	–1.21	–2.44	1.83	3.74	32.27	1.27	0.84	8.50	0.79	0.59	0.72	0.84	5.46	789.95	918.97	702.79	719.14	7.03	7.19
3024805	–2.12	–0.93	2.11	4.94	26.51	1.37	0.72	7.75	0.83	0.90	0.68	0.72	2.86	800.56	891.66	422.40	437.53	4.22	4.38
3024850	–1.40	–1.90	1.75	3.23	35.57	1.32	0.87	7.96	0.76	0.69	0.66	0.87	5.02	783.93	930.19	402.02	417.02	4.02	4.17
3024874	–1.34	–0.21	1.73	4.50	28.40	1.47	0.95	7.57	0.82	0.63	0.68	0.95	4.69	785.47	906.69	291.82	305.98	2.92	3.06
9v3250	–1.84	–0.43	1.70	3.53	33.53	1.32	0.87	8.13	0.78	0.80	0.69	0.87	5.18	779.66	917.69	467.84	483.22	4.68	4.83
9v3270	–2.23	–1.10	1.77	3.32	34.97	1.33	0.83	7.70	0.77	1.07	0.68	0.83	4.43	788.33	933.46	341.63	356.21	3.42	3.56
F3052780	–0.89	0.24	2.57	6.00	22.90	1.23	0.91	8.76	0.86	0.30	0.74	0.91	6.68	736.72	853.49	299.42	313.65	2.99	3.14
F3063064	–0.30	0.43	2.11	5.85	23.35	1.41	0.94	7.82	0.85	0.28	0.72	0.94	5.15	761.08	872.82	226.08	239.51	2.26	2.40
F3063270	–1.30	–0.20	2.79	3.53	33.57	1.27	1.03	10.13	0.78	0.27	0.76	1.03	8.50	733.27	807.01	809.81	826.49	8.10	8.26
F3063430	–1.16	0.78	2.79	6.56	21.37	1.06	0.86	10.10	0.87	0.26	0.84	0.86	8.47	728.79	828.92	687.97	704.28	6.88	7.04
F3152675	–1.31	0.10	2.54	5.38	24.88	1.20	0.95	9.18	0.84	0.32	0.86	0.95	7.51	713.36	835.52	328.62	343.11	3.29	3.43
F3152813	–1.56	0.18	2.76	7.31	19.61	1.10	0.85	10.49	0.88	0.34	0.86	0.85	8.41	759.26	828.82	1431.17	1449.16	14.31	14.49
F3153087	–0.68	0.48	2.43	5.78	23.56	1.20	0.88	8.88	0.85	0.27	0.80	0.88	6.68	732.45	853.32	338.36	352.92	3.38	3.53
F3032833	–1.61	–0.28	1.86	3.19	35.89	1.44	0.90	7.41	0.76	0.73	0.58	0.90	4.28	764.52	916.53	189.33	202.22	1.89	2.02
F3033190	–2.49	–1.25	1.51	4.48	28.46	1.37	0.83	7.88	0.82	1.37	0.66	0.83	4.16	816.87	915.51	694.13	710.46	6.94	7.10
F3033338	–1.69	–0.85	1.79	3.43	34.21	1.31	0.85	8.10	0.77	0.72	0.70	0.85	4.97	763.38	908.40	359.30	374.01	3.59	3.74
F3042790	–1.94	0.77	2.72	5.97	22.98	1.08	0.87	8.87	0.86	0.43	0.77	0.87	7.37	692.59	828.91	181.79	194.57	1.82	1.95
F3043035	–2.57	–0.95	2.37	4.81	27.06	1.23	1.05	8.55	0.83	0.63	0.82	1.05	7.53	677.14	814.78	125.54	137.29	1.26	1.37
F3043288	–2.17	1.11	2.72	7.30	19.62	1.11	0.89	8.90	0.88	0.46	0.79	0.89	7.39	698.10	822.37	199.17	212.22	1.99	2.12
F3142442	–2.44	–0.52	2.47	4.23	29.64	1.17	1.00	8.89	0.81	0.57	0.77	1.00	7.88	683.05	822.10	177.38	190.08	1.77	1.90
F3142558	–1.54	–0.39	1.70	3.40	34.40	1.47	0.90	7.05	0.77	0.74	0.63	0.90	3.87	756.72	914.07	134.68	146.60	1.35	1.47
F3142676	–1.51	–0.53	1.88	3.27	35.26	1.65	0.97	6.65	0.77	0.74	0.65	0.97	3.34	776.16	927.31	105.15	116.52	1.05	1.17
F3142906	–1.61	–0.24	1.78	3.26	35.34	1.31	0.82	8.37	0.77	0.70	0.65	0.82	4.89	799.10	924.93	766.10	782.65	7.66	7.83
F3192560	–0.92	0.33	2.31	3.20	35.77	1.26	0.92	9.17	0.76	0.34	0.72	0.92	6.85	783.64	908.42	904.89	921.82	9.05	9.22
F3193090	–1.49	1.02	2.74	4.50	28.38	1.07	0.81	9.64	0.82	0.35	0.72	0.81	7.50	719.36	848.19	464.94	480.31	4.65	4.80
F3242760	–2.95	0.09	1.64	5.13	25.79	1.19	0.81	7.95	0.84	1.29	0.70	0.81	5.31	726.71	868.99	195.76	208.76	1.96	2.09
F3243300	–2.66	–0.03	1.92	2.96	37.60	1.16	0.89	9.44	0.75	0.82	0.71	0.89	7.45	726.74	867.54	595.28	611.24	5.95	6.11
F3243312	–3.76	–2.87	0.83	4.28	29.43	1.08	0.90	8.57	0.81	2.16	0.82	0.90	7.22	654.31	764.31	221.59	234.96	2.22	2.35
F3222408	–4.54	–2.45	1.26	4.91	26.62	1.18	0.92	8.30	0.83	2.92	0.85	0.92	6.58	688.28	820.80	198.75	211.79	1.99	2.12
F3222707	–2.45	–0.34	2.14	3.59	33.21	1.20	0.93	8.83	0.78	0.66	0.74	0.93	7.11	693.88	833.83	225.32	238.74	2.25	2.39
F3222760	–6.07	–2.46	1.86	5.70	23.83	1.24	1.00	8.71	0.85	5.22	0.76	1.00	7.23	695.35	802.58	222.22	235.60	2.22	2.36
F3232892	–2.34	0.43	1.88	3.44	34.16	1.13	0.87	9.20	0.77	0.67	0.71	0.87	7.31	707.14	846.64	378.56	393.41	3.79	3.93
F3233042	–0.09	0.29	1.77	5.29	25.21	1.42	0.87	7.27	0.84	0.32	0.73	0.87	4.01	773.18	897.71	195.39	208.38	1.95	2.08
F3233310	–2.46	–0.74	2.23	10.07	15.05	1.21	0.85	9.10	0.91	0.80	0.80	0.85	6.44	783.07	835.37	790.84	807.46	7.91	8.07
F3233330	–0.73	–0.21	1.90	6.17	22.42	1.37	0.85	7.31	0.86	0.42	0.77	0.85	4.18	749.86	877.89	141.91	153.98	1.42	1.54
F3282580	–2.29	0.00	1.79	4.33	29.17	1.07	0.82	9.72	0.81	0.70	0.73	0.82	7.66	724.00	846.27	718.10	734.50	7.18	7.35
F3282810	–2.73	–0.05	1.84	4.76	27.23	1.08	0.81	9.67	0.83	0.88	0.71	0.81	7.35	731.11	841.11	738.66	755.12	7.39	7.55
F3283100	–2.80	0.37	1.97	2.80	38.90	1.14	0.83	8.75	0.74	0.94	0.73	0.83	6.48	718.10	893.99	313.17	327.52	3.13	3.28

CIPW after Buckle et al. (2023)						
Qtz	An	Ab	Or	Ap	Ilm	Mag
24.05	11.60	21.40	26.78	1.08	1.91	3.97
20.12	11.85	21.23	30.61	1.13	1.70	4.23
29.88	2.36	27.11	35.50	0.02	0.19	0.80
19.46	10.79	25.13	27.46	1.08	2.07	4.17
24.81	9.04	24.85	28.33	0.87	1.55	3.11
24.49	8.25	24.86	29.47	0.80	1.46	3.12
17.65	7.47	28.20	33.67	0.75	1.40	3.44
29.15	5.18	23.91	37.56	0.07	0.21	1.37
20.78	8.48	24.41	33.44	0.80	1.49	3.30
19.85	8.05	25.56	32.72	0.75	1.45	3.70
21.18	9.96	21.30	31.43	0.82	1.59	3.44
22.39	9.13	24.66	30.22	0.91	1.78	3.50
23.51	12.21	23.58	28.54	0.77	1.72	3.66
21.81	9.19	25.63	30.45	0.70	1.53	3.37
22.77	9.06	23.68	29.37	1.01	1.71	3.66
26.09	6.86	20.84	37.48	0.33	1.01	2.89
25.91	11.04	21.40	31.57	0.44	1.26	3.32
21.74	7.93	22.70	44.30	0.07	0.32	1.05
22.92	2.15	22.64	44.16	0.09	0.50	2.54
26.51	6.25	21.97	39.04	0.12	0.36	2.15
18.04	3.68	23.69	45.67	0.14	0.48	2.87
25.53	6.14	21.99	37.30	0.28	0.71	2.80
26.24	11.37	22.06	28.67	0.75	2.12	2.88
18.84	10.51	26.78	28.29	1.14	2.09	4.08
23.47	8.92	24.66	30.89	0.70	1.24	2.96
30.93	2.53	20.33	38.72	0.07	0.65	2.19
33.21	4.85	21.56	35.77	0.07	0.33	1.45
30.07	3.22	20.35	38.72	0.05	0.65	2.46
31.46	4.86	21.86	37.75	0.07	0.42	1.43
27.75	11.72	22.26	26.45	0.63	1.69	2.93
27.38	14.28	19.72	25.88	0.80	1.73	3.16
19.03	9.04	25.67	31.87	0.75	1.80	3.41
19.38	8.15	23.78	38.37	0.31	1.16	2.96
24.88	2.23	21.93	41.92	0.12	0.82	2.15
28.21	5.31	25.68	29.44	0.19	1.23	2.84
23.18	5.20	27.48	36.90	0.09	0.71	1.76
30.93	2.77	39.76	23.08	0.02	0.15	0.68
30.02	5.56	31.33	27.60	0.05	0.27	1.57
29.24	5.96	23.92	35.80	0.07	0.48	1.38
29.27	7.17	25.85	33.67	0.09	0.48	1.48
26.16	4.15	27.24	35.68	0.07	0.63	1.58
25.61	10.81	22.37	27.62	0.86	1.41	3.83
20.14	6.54	24.09	37.47	0.44	1.00	3.96
28.01	9.59	21.41	28.42	0.70	1.07	3.59
22.53	2.32	29.65	36.96	0.12	0.76	2.03
22.15	2.75	28.93	37.20	0.12	0.84	2.09
26.26	4.26	25.01	34.52	0.09	0.80	2.17

Table 2. Analysis of major elemental relationships in tripartite rapakivi samples. Multi-dimensional discriminant functions DF1 and DF2, based on tectonic discrimination after Verma (2013), are defined as follows: DF1 = 0.051 $\ln(TiO_2/SiO_2)$ + 0.226 $\ln(Al_2O_3/SiO_2)$ − 1.77 $\ln(Fe_2O_3/SiO_2)$ + 1.83 $\ln(FeO/SiO_2)$ − 0.065 $\ln(MnO/SiO_2)$ + 0.134 $\ln(MgO/SiO_2)$ + 0.225 $\ln(CaO/SiO_2)$ + 0.742 $\ln(Na_2O/SiO_2)$ − 1.78 $\ln(K_2O/SiO_2)$ + 0.146 $\ln(P_2O_5/SiO_2)$ − 2.12, and DF2 = 1.09 $\ln(TiO_2/SiO_2)$ − 1.65 $\ln(Al_2O_3/SiO_2)$ − 1.19 $\ln(Fe_2O_3/SiO_2)$ + 1.03 $\ln(FeO/SiO_2)$ + 0.82 $\ln(MnO/SiO_2)$ + 0.026 $\ln(MgO/SiO_2)$ + 0.023 $\ln(CaO/SiO_2)$ + 0.212 $\ln(Na_2O/SiO_2)$ + 0.085 $\ln(K_2O/SiO_2)$ − 0.85 $\ln(P_2O_5/SiO_2)$ + 2.54. Major-element ratios include K_2O/Na_2O (potassium oxide to sodium oxide weight ratio), FeO*/MgO (total iron expressed as ferrous iron to magnesium oxide ratio), Mg#[wt.%] = 100 × [MgO/(MgO + FeO*)] (magnesium number), and MALI (wt.%) = (Na_2O + K_2O) − CaO (modified alkali-lime index). Aluminosity indices are expressed as A/NK [mol] = $Al_2O_3/(Na_2O + K_2O)$ (molar aluminosity index) and ASI [mol] = $Al_2O_3/(CaO + Na_2O + K_2O)$ (aluminum saturation index), with total alkalis given by $Na_2O + K_2O$. Iron enrichment is quantified using FeO*/(FeO* + MgO) (total iron enrichment index). Fe^{3+}#[wt.%] = $Fe_2O_3/(FeO + Fe_2O_3)$ (iron number enrichment). X_{Mag} = Mag/(Mag + Ilm) (proportion of magnetite relative to total iron-titanium oxides). The alkali indices are referenced as TAS (total alkali-silica), MALI (modified alkali-lime index), and ASI (aluminum saturation index). Temperature estimates are reported as $TSiO_2$ (°C) and T_{MgO} (°C), while pressure conditions are constrained using P_{Qz} (MPa) and $P_{Ab–Or}$ (MPa) (pressure in megapascals) and P_{Qz} and $P_{Ab–Or}$ (kbar) (pressure in kilobars). Normative mineralogy is derived from CIPW calculations and includes Qtz (quartz), An (anorthite), Ab (albite), Or (orthoclase), Ap (apatite), Ilm (ilmenite), and Mag (magnetite)

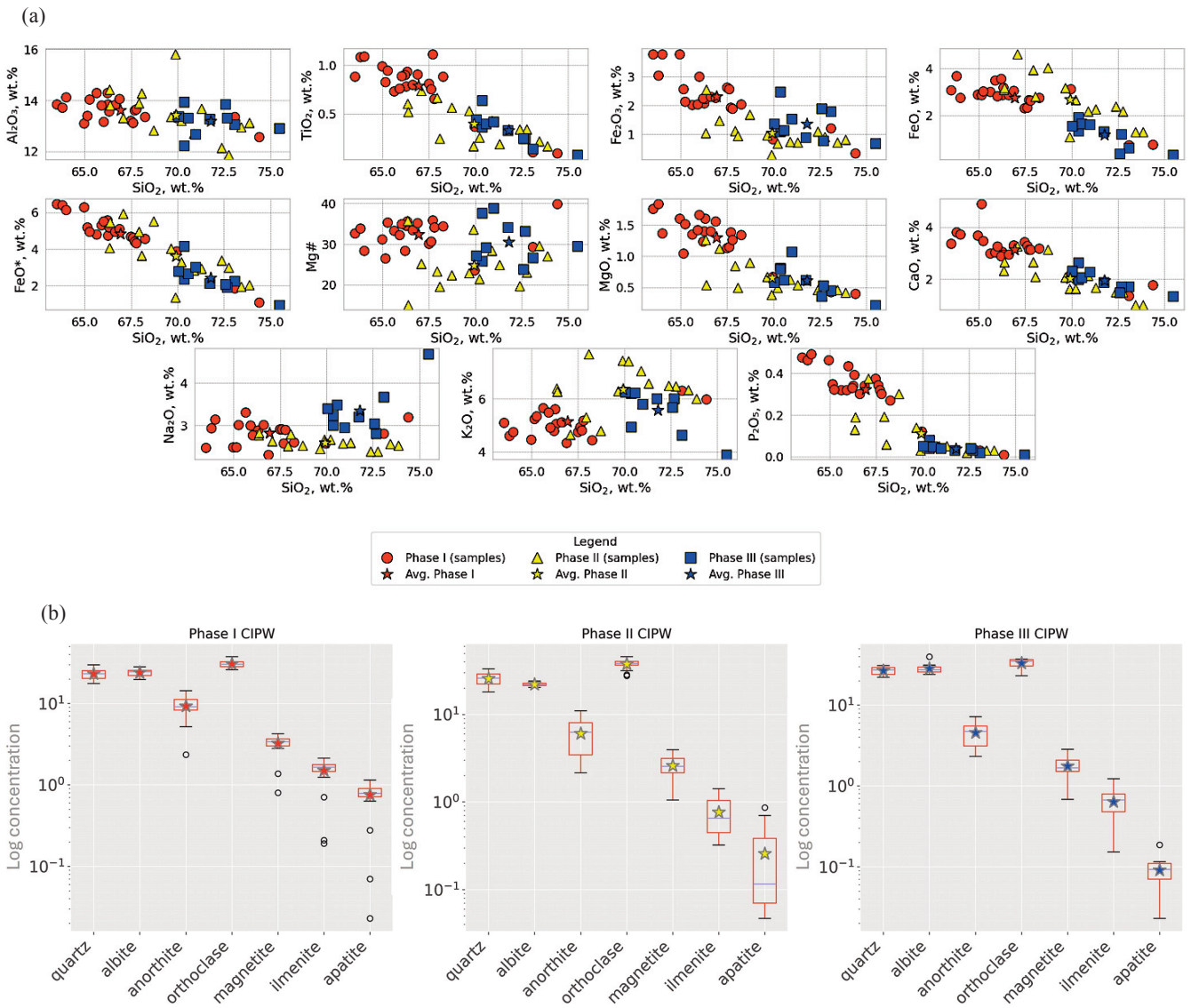

Fig. 2. **(a)** Major-element-normalized distributions of samples from the Kivisilla et al. (1999) dataset and this study, categorized into three magmatic phases of the analyzed rapakivi granites. Harker biplots illustrate relationships between SiO_2 and selected major elements. **(b)** Boxplots of CIPW normative values for the tripartite phases.

TiO_2 and iron oxides decrease systematically from Phase I to Phase III. Average TiO_2 contents decline from 0.79 wt.% (0.10–1.11 wt.%) in Phase I to 0.40 wt.% (0.17–0.74 wt.%) in Phase II and 0.33 wt.% (0.08–0.64 wt.%) in Phase III. Ferric iron (Fe_2O_3, Fe^{3+}) decreases from 2.30 wt.% (0.35–3.77 wt.%) in Phase I to 1.05 wt.% (0.29–2.54 wt.%) in Phase II, followed by a slight increase to 1.37 wt.% (0.69–2.47 wt.%) in Phase III, whereas ferrous iron (FeO, Fe^{2+}) declines from 2.75 wt.% (0.75–3.68 wt.%) in Phase I to 2.67 wt.% (1.09–4.61 wt.%) in Phase II and 1.19 wt.% (0.32–1.92 wt.%) in Phase III. When expressed as total iron (FeO*), recalculated from measured FeO and Fe_2O_3 (Table 2), average values decrease from 4.82 wt.% (1.07–6.46 wt.%) in Phase I to 3.62 wt.% (1.35–5.93 wt.%) in Phase II and 2.42 wt.% (0.94–4.14 wt.%) in Phase III.

Mg# decreases from 32.46 (23.56–39.89) in Phase I to 24.79 (15.05–35.77) in Phase II, followed by a partial increase to 30.59 (23.83–38.90) in Phase III. MgO shows a more uniform decline, decreasing from 1.30 wt.% (0.40–1.84 wt.%) in Phase I to 0.65 wt.% (0.38–1.26 wt.%) in Phase II and 0.61 wt.% (0.22–1.08 wt.%) in Phase III. CaO decreases from 3.13 wt.% (1.35–4.89 wt.%) in Phase I to 2.02 wt.% (1.01–3.26 wt.%) in Phase II and 1.94 wt.% (1.34–2.64 wt.%) in Phase III, whereas alkali-related oxides record progressive fractionation. Na_2O increases from 2.82 wt.% (2.31–3.31 wt.%) in Phase I and 2.59 wt.% (2.38–2.82 wt.%) in Phase II to 3.35 wt.% (2.81–4.68 wt.%) in Phase III. K_2O rises from 5.15 wt.% (4.34–6.32 wt.%) in Phase I to a maximum of 6.35 wt.% (4.65–7.70 wt.%) in Phase II, before decreasing slightly to 5.57 wt.% (3.89–6.26 wt.%) in Phase III.

Accessory-controlled components show range contractions and declining averages: P_2O_5 decreases from 0.32 wt.% (0.01–0.49 wt.%) in Phase I to 0.11 wt.% (0.02–0.37 wt.%) in Phase II and 0.04 wt.% (0.01–0.08 wt.%) in Phase III, while average SO_3 decreases from 0.27 wt.% in Phase I to 0.23 wt.% in Phases II and III.

Average LOI decreases from 0.70 wt.% in Phase I to 0.47 wt.% in Phase III, consistent with progressive differentiation; however, LOI is not interpreted as a primary magmatic parameter because it may reflect secondary alteration.

4.2. CIPW normative trends

The distribution of CIPW normative values per phases is shown in Fig. 3. Normative quartz increases modestly with magmatic evolution, from 23.19% (17.65–29.88%) in Phase I to 25.66% (18.04-33.21%) in Phase II, reaching 26.79% (22.15–30.93%) in Phase III. Phosphate phases show a pronounced depletion with differentiation. Normative apatite decreases from 0.75% (0.02–1.14%) in Phase I to 0.26% (0.05–0.86%) in Phase II and 0.09% (0.02–0.19%) in Phase III.

Feldspars show a differentiated, non-monotonic evolutionary trend. Normative albite decreases slightly, from 24.03% (19.72–28.20%) in Phase I to 22.06% (20.33–24.09%) in Phase II, followed by a marked increase to 28.48% (23.92–39.76%) in Phase III. In contrast, anorthite declines systematically from 9.30% (2.36–14.28%) in Phase I to 6.05% (2.15–11.04%) in Phase II and 4.54% (2.32–7.17%) in Phase III. Orthoclase reaches its maximum abundance in Phase II at 37.80% (27.62–45.67%), compared to 30.68% (25.88–37.56%) in Phase I and 33.08% (23.08–37.20%) in Phase III.

Oxide phases decrease progressively through the magmatic sequence. Normative magnetite diminishes from 3.23% (0.80–4.23%) in Phase I to 2.59% (1.05–3.96%) in Phase II and 1.76% (0.68–2.84%) in Phase III. Ilmenite follows a similar trend, decreasing from 1.51% (0.19–2.12%) in Phase I to 0.76% (0.32–1.41%) in Phase II and 0.63% (0.15–1.23%) in Phase III.

A correlation matrix of CIPW normative mineral compositions for the Märjamaa and Kloostri granitoids (Fig. 3) highlights systematic mineralogical normative associations across Phases I–III. Correlation strengths are expressed as Pearson correlation coefficients (r).

Phase I (Fig. 3a) shows strong negative correlations between normative quartz and Fe–Ti–P phases, including magnetite (r = –0.77), ilmenite (r = –0.54), and apatite (r = –0.66), while quartz–feldspar correlations are weak (albite r = –0.36, anorthite r = –0.22, orthoclase r = 0.09). Albite shows weak negative correlations with oxide-phosphate phases (magnetite r = –0.14, ilmenite r = –0.19, apatite r = –0.14). Anorthite is positively correlated with magnetite (r = 0.70), ilmenite (r = 0.83), and apatite (r = 0.73). Orthoclase shows strong negative correlations with anorthite (r = –0.85) and with oxide-phosphate phases (magnetite r = –0.57, ilmenite r = –0.82, apatite r = –0.73). Magnetite, ilmenite, and apatite are strongly positively correlated (magnetite–ilmenite r = 0.85, magnetite–apatite r = 0.93, ilmenite–apatite r = 0.90).

Phase II (Fig. 3b) retains negative quartz–oxide correlations, but with reduced magnitudes relative to Phase I (magnetite r = –0.38, ilmenite r = –0.21, apatite r = –0.16). Quartz shows a strong negative correlation with albite (r = –0.83), while albite exhibits weak positive correlations with anorthite (r = 0.14), magnetite (r = 0.25), and apatite (r = 0.14). Anorthite remains positively correlated with magnetite (r = 0.47), ilmenite (r = 0.65), and apatite (r = 0.78). Orthoclase maintains strong negative correlations with anorthite (r = –0.72) and oxide-phosphate phases (magnetite r = –0.54, ilmenite r = –0.69, apatite r = –0.81) and reaches its highest normative proportions in Phase II. Magnetite, ilmenite, and apatite remain strongly positively correlated (magnetite–ilmenite r = 0.83, magnetite–apatite r = 0.81, ilmenite–apatite r = 0.84).

Phase III (Fig. 3c) shows a reorganized correlation structure relative to Phases I and II, with changes in feldspar–oxide relationships. Quartz remains negatively correlated with oxide-phosphate phases (magnetite r = –0.47, ilmenite r = –0.55, apatite r = –0.42), shows a moderate positive correlation with anorthite (r = 0.49), and a strong negative correlation with orthoclase (r = –0.77). Albite shows negative correlations with all major phases, including anorthite (r = –0.54), orthoclase (r = –0.70), magnetite (r = –0.60), ilmenite (r = –0.59), and apatite (r = –0.55), and reaches its highest normative proportions in Phase III. Anorthite shows near-zero correlations with oxide-phosphate phases (magnetite r = 0.01, ilmenite r = –0.08, apatite r = 0.05). Orthoclase shows positive correlations with magnetite (r = 0.37), ilmenite (r = 0.45), and apatite (r = 0.35). Magnetite, ilmenite, and apatite remain strongly positively correlated (magnetite–ilmenite r = 0.94, magnetite–apatite r = 0.92, ilmenite–apatite r = 0.95).

5. Petrogenesis

5.1. A-type affinity and major-element evolution

Sample distributions along the $CaO/(FeO + MgO + TiO_2)$ vs. Al_2O_3 trend confirm an A-type affinity (Fig. S2a; Dall'Agnol and de Oliveira 2007). The Al_2O_3 contents of the samples fall within the usual A-type interval of 11–14 wt.%, though elevated values reaching 17 wt.% have been documented in certain rapakivi suites (Dall'Agnol and de Oliveira 2007; Duchesne et al. 2010; Grabarczyk et al. 2023), as it is observed in some Phase I and II samples. In An–Ab–Or (Barker 1979; Luo et al. 2024) and total alkali-silica (TAS) diagrams (Figs 4a and S2b; Le Maitre 2002), Märjamaa and Kloostri compositions evolve from quartz monzonite-granodiorite fields (Phase I) to granite fields (Phases II–III), consistent with Fennoscandian rapakivi trends (Rämö and Haapala 1995; Kosunen 1999; Haapala et al. 2005). Total alkalis ($Na_2O + K_2O$) increase from Phase I to Phase III, paralleling Finnish rapakivi suites (Fig. S2b).

Samples range from alkali-calcic to alkali compositions (MALI > 3.8) and are predominantly metaluminous (ASI < 1.0) (Table 2). Phase I is moderately alkaline, with MALI values of 4.84 (2.86–7.77) and ASI of 0.86 (0.72–0.97). Phase II shows increased alkalinity, with MALI reaching 6.93 (4.01–8.05) and slightly higher ASI values of 0.91 (0.81–1.05). Phase III maintains similarly high alkalinity, with MALI of 6.97 (5.31–7.66) and ASI of 0.88 (0.81–1.00), indicating dominantly metaluminous to marginally peraluminous compositions (Table 2; Figs 4b and S2d).

In the $K_2O–SiO_2$ diagram (Rickwood 1989), the samples fall within the high-K alkaline series and overlap the field of Finnish rapakivi granitoids (Fig. S2c; Rämö and Haapala 1995, 2005; Kosunen 1999). In the geochemical discrimination diagrams of Frost et al. (2001), the analyzed samples are located in the ferroan A-type granite field (Fig. 4c,d), coinciding with the compositional range of typical Finnish rapakivi

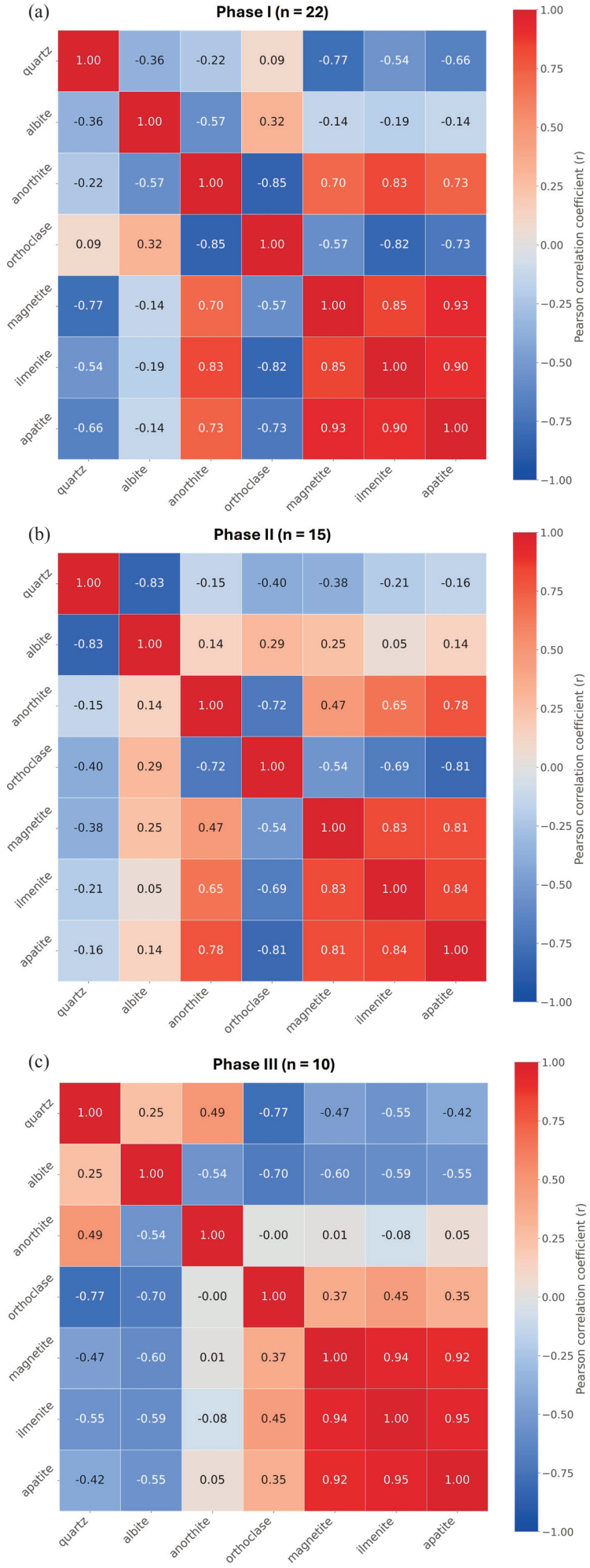

Fig. 3. Comparative analysis of mineral correlation matrices across three phases: **(a)** Phase I matrix, **(b)** Phase II matrix, and **(c)** Phase III matrix.

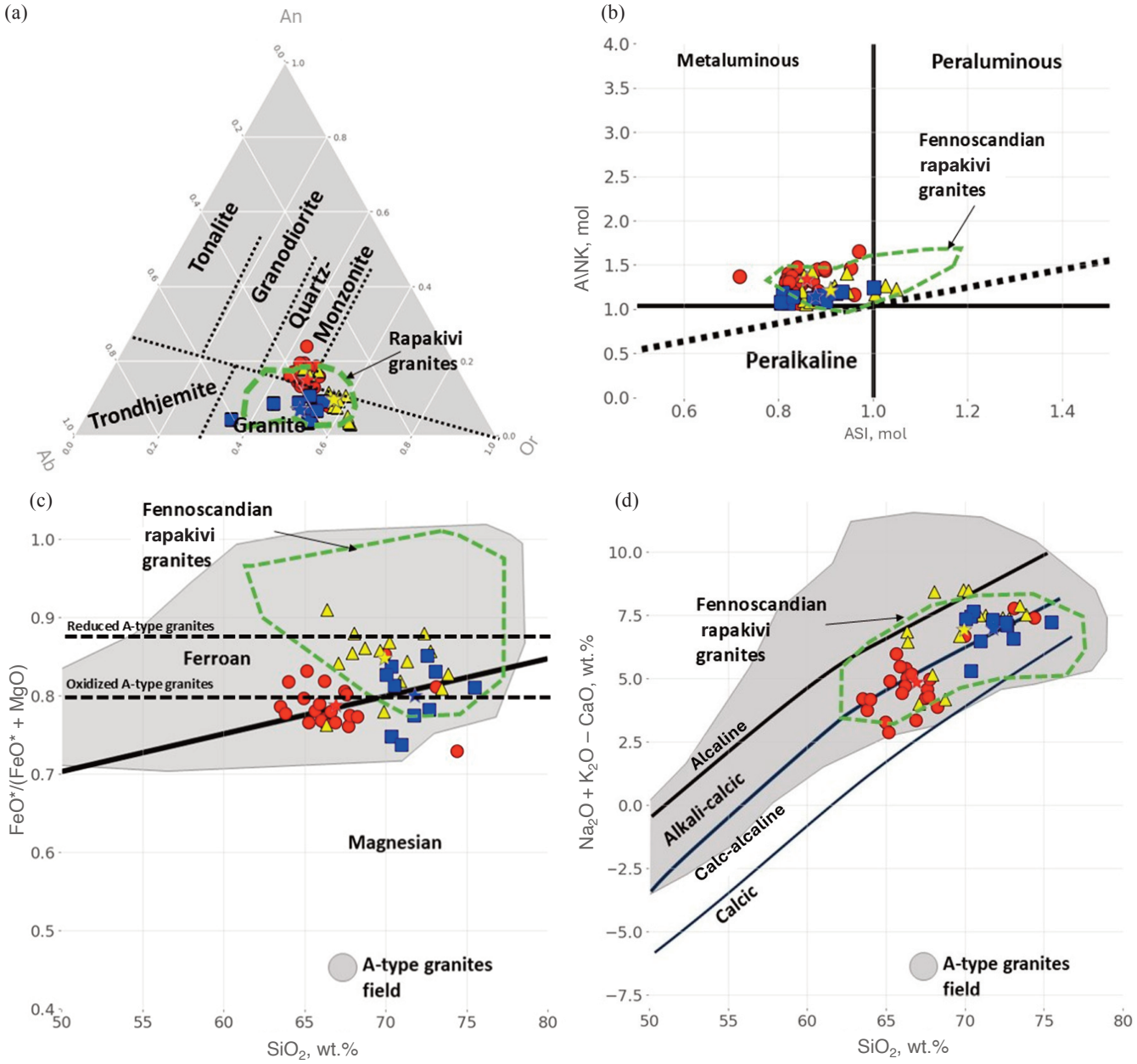

Fig. 4. Geochemical classification of the Märjamaa and Kloostri tripartite phases of rapakivi granitoids. **(a)** An–Ab–Or diagram from Barker (1979), with rapakivi classification after Luo et al. (2024). **(b)** A/NK vs. ASI diagram from Maniar and Piccoli (1989). **(c)** $FeO^*/(FeO^* + MgO)$ vs. SiO_2 diagram after Frost et al. (2001), modified from Hinchey et al. (2024). **(d)** ($Na_2O + K_2O - CaO$) vs. SiO_2 diagram after Frost et al. (2001). Sources of Fennoscandian rapakivi plutons are based on the work of Dall'Agnol and de Oliveira (2007) and Grabarczyk et al. (2023), utilizing results from Rämö and Haapala (1995, 2005) for the Wiborg area, Kosunen (1999) for the Bodom and Obbnäs rapakivi plutons, Heinonen et al. (2010) for the Ahvenisto body, and Sharkov (2010) for the Salmi granitoids. For legend symbols, see Table 2.

granites (Soesoo and Hade 2012; Grabarczyk et al. 2023; Hinchey et al. 2024).

FeO^*/MgO ratios constrain melt evolution, with values <4 indicating weak fractionation and values of 4–16 characteristic of fractionated A-type felsic granites (Whalen et al. 1987; Bonin 2007). Phase I shows a low average ratio of 3.78 (2.69–5.78), consistent with limited fractionation, whereas Phase II reaches a higher average ratio of 5.75 (3.20–10.07), indicating peak fractionation; Phase III displays an intermediate ratio of 4.19 (2.80–5.70), reflecting moderate differentiation.

These phase-dependent fractionation patterns are evident in the organization of CIPW normative correlations (Figs 2b and 3). Phase I (Fig. 3a) shows negative quartz–oxide correlations and positive anorthite–Fe–Ti–P coupling. Phase II (Fig. 3b) shows weaker quartz–oxide correlations, peak orthoclase, and negative orthoclase–oxide relationships. Phase III (Fig. 3c) shows reorganization, with strongest magnetite–ilmenite–apatite correlations, peak albite, positive orthoclase–oxide associations, and decoupling of anorthite from oxide-phosphate phases, consistent with late-stage Na enrichment.

In the multidimensional tectonic discrimination diagram of Verma et al. (2013), defined by DF1 and DF2 (Table 2; Fig. 5c), most samples plot within the continental rift field, with minor overlap into the collision domain. These results should be interpreted cautiously, as major-element discriminant functions may yield ambiguous tectonic classifications

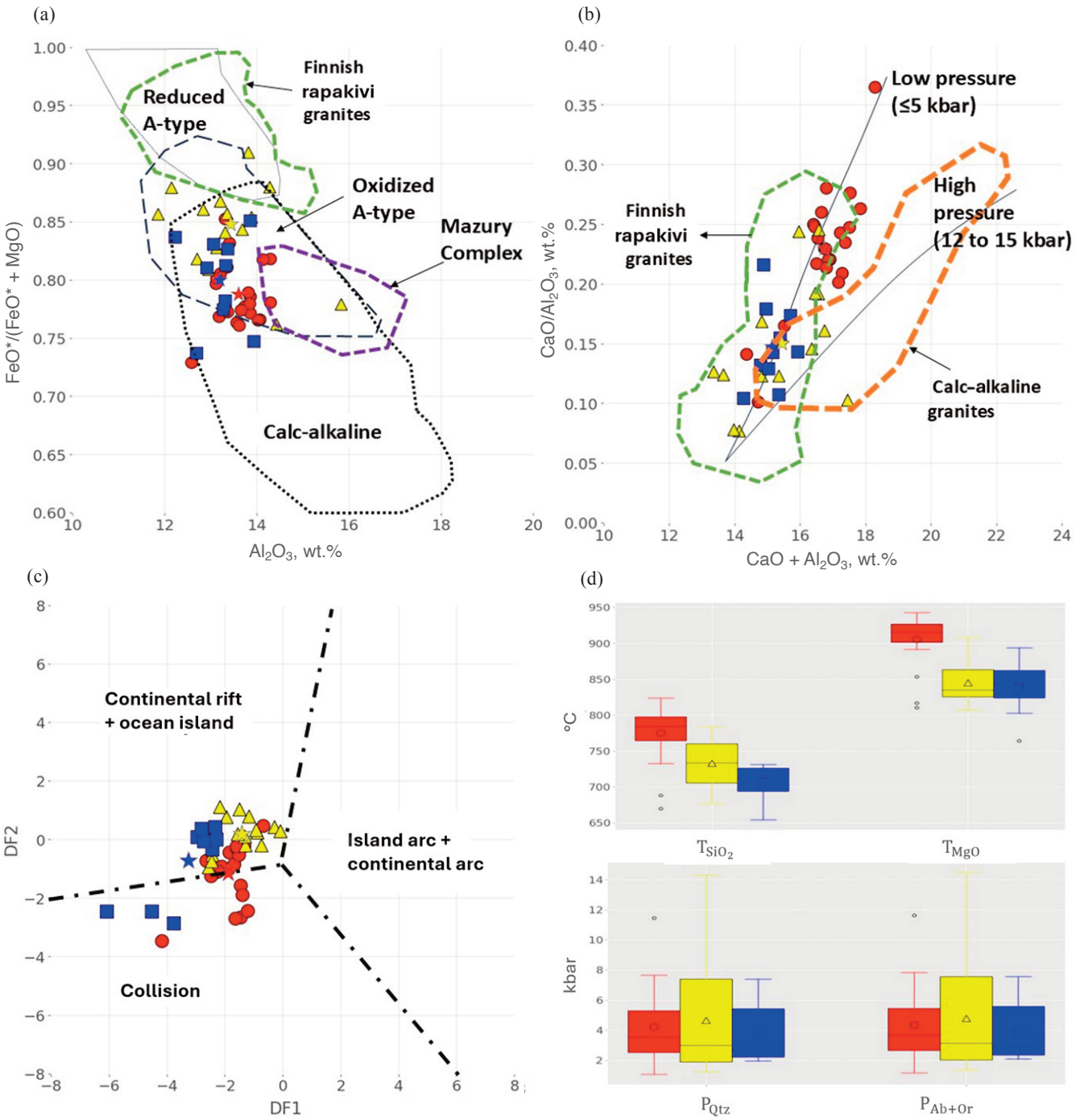

Fig. 5. Petrogenetic classification diagrams for the tripartite Märjamaa and Kloostri rapakivi granite phases. **(a)** FeO*/(FeO* + MgO) vs. Al_2O_3 classification plot of calc-alkaline and A-type granites, including fields for reduced and oxidized subtypes, based on Dall'Agnol and de Oliveira (2007). **(b)** Whole-rock CaO/Al_2O_3 vs. CaO + Al_2O_3 for pressure ranges in A-type granites, after Patiño Douce (1997, 1999), modified from Dall'Agnol and de Oliveira (2007). Sources of the Finnish rapakivi plutons are derived from the work of Dall'Agnol and de Oliveira (2007) and references therein, while the domain corresponding to the Mazury Complex domain follows Grabarczyk et al. (2023). **(c)** Tectonic discriminant-function (DF1 and DF2; Table 2) multidimensional diagrams based on log-transformed major- and trace-element ratios for tectonic discrimination of acid granitic rocks, after Verma et al. (2013). **(d)** Boxplots of T–P estimates from T_{SiO_2} and T_{MgO}, and P_{Qtz} and P_{Ab+Or} calibrations. For legend symbols, see Table 2.

(Verma et al. 2013, 2022) and must be evaluated alongside independent geological, geochemical, and geophysical constraints (e.g., Soesoo and Niin 1992; Soesoo 1993; Klein et al. 1994; Kirs et al. 2004; Solano-Acosta et al. 2025b). When considered in this broader context, the observed distribution is consistent with a transtensional–transpressional tectonic regime during Märjamaa and Kloostri emplacement, as proposed by Solano-Acosta et al. (2025b). Additional constraints from associated mafic magmatism and deeper crustal sources are required to develop a fully integrated tectono-petrogenetic model and are deferred to future work (Verma et al. 2022).

5.2. Redox evolution and Fe–Ti oxide systematics

A-type granites in the Laurentia–Baltica region are commonly classified into ilmenite-, magnetite-, and two-mica (peralumi-

nous) series (Ishihara 1977; Anderson and Morrison 2005; Dall'Agnol and de Oliveira 2007). In Laurentia, magnetite-series granites typically show $FeO^*/(FeO^* + MgO)$ ratios of 0.80–0.88, whereas ilmenite-series granites generally exceed 0.88, reflecting comparatively reduced conditions (Frost and Frost 1997; Anderson and Morrison 2005). Finnish rapakivi granites span a broader range (0.79–1.00) and are commonly associated with reduced A-type affinities (Rämö and Haapala 1995, 2005; Grabarczyk et al. 2023), although their relationship to oxidized A-type granitoids remains debated (Bonin 2007; Dall'Agnol and de Oliveira 2007; Dall'Agnol et al. 2012). Accordingly, the Märjamaa and Kloostri intrusions plot predominantly within oxidized A-type fields, with $FeO^*/(FeO^* + MgO)$ ratios of 0.73–0.85 (avg. 0.79) in Phase I, 0.76–0.91 (avg. 0.84) in Phase II, and 0.74–0.85 (avg. 0.80) in Phase III. All phases occupy oxidized domains in Fig. 4c (Frost et al. 2001; Hinchey et al. 2024) and equivalent fields in Fig. 5b (Dall'Agnol and de Oliveira 2007), although Phase II clusters closest to the reduced boundary.

The classification and redox interpretation of A-type granites remain controversial, particularly for oxidized, magnetite-bearing varieties sensu Anderson and Bender (1989) and Dall'Agnol and de Oliveira (2007). Although Fe–Mg-based discrimination diagrams are widely used in granitoid studies, they integrate both Fe^{2+} and Fe^{3+} and are strongly influenced by magmatic differentiation. In the Märjamaa–Kloostri system, $FeO^*/(FeO^* + MgO)$ primarily reflects bulk iron enrichment relative to Mg rather than redox conditions. Consistently, Mg values define a pronounced minimum in Phase II and higher averages in Phases I and III, indicating phase-dependent Fe–Mg partitioning during differentiation rather than changes in oxidation state or magma source.

Preferentially, geochemical characterization should be accompanied by petrographic, Fe–Ti oxide, and magnetic susceptibility studies (Dall'Agnol and de Oliveira 2007). Redox conditions are best constrained by whole-rock iron speciation, quantified as the molar ferric iron fraction, $Fe^{3+}\# = Fe_2O_3/(FeO + Fe_2O_3)$ (Table 2; Yang et al. 2021). This parameter tracks variations in redox state independently of total iron content or magmatic differentiation. The smaller the $Fe^{3+}\#$ value of a granite, the lower the redox conditions under which it formed (Ishihara 1977, 1981, 2004). A $Fe^{3+}\#$ value of ~0.1 corresponds to very reduced conditions, values in the range ~0.1–0.3 indicate reduced redox states, intermediate values of ~0.3–0.5 define transitional conditions, and values > 0.5 reflect oxidized conditions, with $Fe^{3+}\#$ approaching 1.0 representing strongly oxidized compositions (Ishihara et al. 2000; Ishihara 2004; Yang et al. 2021). In the analyzed samples, average $Fe^{3+}\#$ values increase from Phase II (0.28; 0.21–0.44), which predominantly falls within the reduced to lower transitional range, through Phase I (0.45; 0.21–0.62), spanning transitional to weakly oxidized conditions, to Phase III (0.54; 0.40–0.84), which is dominantly oxidized.

Contrasting this with the CIPW normative Fe–Ti oxide systematics, all phases are magnetite-dominant (Fig. 2b); however, the absolute abundances of both magnetite and ilmenite decrease systematically from Phase I to Phase III. The magnetite fraction (X_{Mag} = Mag/(Mag + Ilm); Table 2) increases from Phase I (avg. 0.69) to Phase II (avg. 0.78) before slightly decreasing in Phase III (avg. 0.75). This non-monotonic behavior does not necessarily reflect changes in oxidation state. Instead, the Phase II maximum in X_{Mag} may result from ilmenite being more strongly suppressed than magnetite, as TiO_2 availability decreases during magmatic differentiation beginning in Phase I (Fig. 2a), which limits ilmenite crystallization. Additionally, the modest increase observed in Phase III may partly reflect higher Fe_2O_3. Therefore, X_{Mag} remains primarily controlled by Fe–Ti partitioning during differentiation rather than serving as a direct redox proxy.

5.3. Theoretical thermobarometric constraints

Based on experimental data (Patiño Douce 1997, 1999), A-type granites form through low-pressure (≤ 5 kbar) hybridization of calc-alkaline granitoids with high-Al olivine tholeiites or metagraywackes, producing melts with plagioclase and orthopyroxene as residual phases (Dall'Agnol and de Oliveira 2007). Our samples plot along this low-pressure trend in the CaO/Al_2O_3 vs. $CaO + Al_2O_3$ diagram (Fig. 5b), consistent with Finnish rapakivi granites. In contrast, higher-pressure (12–15 kbar) melts yield clinopyroxene-rich residues and plot within the calc-alkaline granitoid field (Dall'Agnol and de Oliveira 2007).

Yang (2017) proposed two equations to estimate crystallization pressure in (haplo-)granitic magmas based on normative quartz, albite, and orthoclase contents. The equations are $P_{Qtz} = -0.2426 \times Qtz^3 + 26.392 \times Qtz^2 - 980.74 \times Qtz + 12563$ and $P_{Ab+Or} = 0.2426 \times (Ab + Or)^3 - 46.397 \times (Ab + Or)^2 + 2981.3 \times (Ab + Or) - 64224$, where P is the pressure in MPa. Normalized CIPW quartz, albite, and orthoclase were used for the calculations. Pressure estimates derived from P_{Qz} are systematically very close to those obtained from P_{Ab+Or}, showing a strong correspondence between both approaches ($R^2 \approx 0.9$; Yang 2017).

Average pressures derived from P_{Qtz} are 4.20 kbar (1.05–11.45 kbar) for Phase I, 4.64 kbar (1.26–14.31 kbar) for Phase II, and 3.81 kbar (1.96–7.39 kbar) for Phase III, with comparable results obtained from the P_{Ab+Or} formulation (Table 2; Fig. 5d). These values indicate predominantly mid-crustal crystallization across all phases. The highest pressures in Phase I (11.45 kbar; sample 3023700) and Phase II (14.31 kbar; sample F3043288) are each defined by a single sample and are not representative of typical conditions. As noted by Yang (2017) and Yang et al. (2021), these normative barometers are calibrated for granitic compositions containing 15–40 wt.% normative quartz and are sensitive to extreme quartz and alkali feldspar proportions, as well as to melt composition (e.g., CaO, FeO, MgO, and volatiles).

Although Phase II yields slightly higher average pressures than Phases I and III, this difference is interpreted as a compositional effect, with additional sensitivity to redox-dependent normative quartz–feldspar systematics, rather than a genuine increase in crystallization depth. Phase II is characterized by advanced feldspar-dominated differentiation,

reduced CaO contents, and lower Fe^{3+}# values, conditions that are known to bias quartz-based barometric estimates toward higher pressures in metaluminous granites. Because redox conditions modulate normative quartz–feldspar systematics, the resulting pressure estimates are best interpreted in a comparative, phase-relative sense rather than as exact absolute depths. Accordingly, the isolated high-pressure estimates are interpreted as artefacts of calibration sensitivity near compositional limits rather than evidence for sustained lower-crustal crystallization.

Duan et al. (2022) criticized zircon-saturation thermometry for estimating magma temperatures because of the limited influence of Zr in rock compositions, despite its use in rapakivi studies (e.g., Grabarczyk et al. 2023). They proposed two formulas for granitoid studies: T_{SiO_2} [°C] = –14.16 × SiO_2 [wt.%] + 1723 and T_{MgO} [°C] = 887.6 × (MgO [wt.%])$^{0.0989}$, which approximate temperatures of melt-crystal mixtures prior to solidification (Duan et al. 2022).

T_{SiO_2} decreases systematically from Phase I (775.15 °C) through Phase II (732.83 °C) to Phase III (706.56 °C) (Fig. 5d), consistent with progressive cooling during differentiation and increasing silica enrichment, also reflected by rising normative quartz contents (Table 2). T_{MgO} estimates are systematically higher but likewise decline from Phase I to Phase III (from 905.82 °C to 845.49 °C and 838.60 °C). The less regular evolution of T_{MgO} reflects its stronger sensitivity to the availability of Mg-bearing and Fe–Ti–P phases, consistent with the progressive normative depletion of anorthite, magnetite, ilmenite, and apatite and the reorganization of mineral correlations in the more evolved assemblages (Figs 2b and 3a–c). In contrast, T_{SiO_2} more directly tracks bulk melt evolution and thus records a smoother cooling trend.

6. Discussion

Major-element systematics define a coherent, multistage differentiation sequence in the Märjamaa–Kloostri rapakivi system, evolving from a ferroan, oxide-phosphate-enriched Phase I through a strongly fractionated, K-rich Phase II to a highly evolved, quartz–feldspar–Na-dominated Phase III. This evolution is marked by increasing silica and alkalis, and by depletion of the Fe–Ti–Mg–Ca-bearing and phosphate components, while Al_2O_3 remains broadly stable, indicating feldspar-controlled differentiation. Redox evolution progresses from moderately oxidized Phase I through comparatively reduced Phase II to an oxide-poor but most oxidized Phase III. Thermometric estimates indicate progressive cooling, whereas pressures cluster within mid-crustal conditions, supporting differentiation within a single reservoir. Together, these data define a multistage rapakivi system in which oxide abundance tracks differentiation, while redox variations reflect phase-specific pathways rather than a monotonic trend.

Fractionation intensity, as indicated by the FeO^*/MgO ratio, reveals that Phase II is the most fractionated felsic end-member, while Phase I shows less evolved compositions. Petrographic observations confirm that Phase I is the densest and darkest, Phase II is more felsic and mainly biotite (with some muscovite), and Phase III is leucocratic (Soesoo and Niin 1992; Klein et al. 1994). In Märjamaa, porphyritic textures with microcline phenocrysts, zoned oligoclase–andesine, and multiple quartz generations indicate progressive silica enrichment and reduced calcic components during differentiation (Klein et al. 1994). Normative systematics further indicate depletion of oxide- and phosphate-bearing assemblages, reflecting progressive exhaustion of accessory phases during differentiation.

On multidimensional discriminant diagrams, the Märjamaa–Kloostri granitoids plot predominantly within the continental rift domain (Fig. 5c), consistent with intracontinental extension or transtensional reactivation along the Laurentia–Baltica margin (Verma et al. 2013, 2022; Solano-Acosta et al. 2025b). Emplacement coincides with the late stages of the Fennoscandian rapakivi AMCG event (Wiborg suite) and is linked to asthenospheric upwelling and mafic underplating during Nuna superswell dynamics (Ahl et al. 1997; Vigneresse 2005; Sharkov 2010; Pirajno and Santosh 2015; Salminen et al. 2021; Solano-Acosta et al. 2025b).

Major-element indices underpin A-type granite classification and provide insights into magma sources and redox conditions (Frost et al. 2001; Bonin 2007; Dall'Agnol et al. 2012). These granitoids are subdivided into reduced and oxidized suites controlled by oxygen fugacity (fO_2), water content, and source characteristics (Ishihara 1977; Frost and Frost 1997; Vigneresse 2005; Dall'Agnol and de Oliveira 2007). Oxidized A-type magmas are associated with hydrous lower-crustal sources and magnetite-bearing assemblages crystallizing near the nickel–nickel oxide (NNO) buffer, reflecting relatively high fO_2 conditions linked to Proterozoic increases in atmospheric and fluid O_2 (Vigneresse 2005; Dall'Agnol and de Oliveira 2007; Grabarczyk et al. 2023), whereas most A-type granites crystallize under redox conditions close to fayalite–magnetite–quartz (FMQ), with reduced fayalite–ilmenite assemblages dominant and magnetite-bearing variants representing more oxidized end-members (Frost and Frost 1997, 2011; Dall'Agnol et al. 2012). On the oxygen fugacity scale, NNO is more oxidizing than FMQ and iron–wüstite buffers, but less oxidized than the hematite–magnetite buffer (Frost and Frost 1997; Dall'Agnol and de Oliveira 2007; Campbell et al. 2009).

Experimental and petrological studies show that, in addition to pressure, the geochemical character of A-type granites is strongly controlled by oxygen fugacity and magma source properties, including water content (Frost and Frost 1997; Frost et al. 1999; Dall'Agnol and de Oliveira 2007). Oxidized A-type granites are commonly interpreted to derive from hydrous lower-crustal quartz–feldspathic igneous sources under relatively oxidizing conditions, favoring clinopyroxene-bearing residues during dehydration melting and producing less canonical A-type major-element signatures (Dall'Agnol et al. 1999; Anderson and Morrison 2005). In contrast, reduced A-type granites may originate from more reduced quartz–feldspathic sources, potentially involving a metasedimentary component, or from differentiated tholeiitic

magmas (Frost and Frost 1997; Frost et al. 1999; Anderson and Morrison 2005; Dall'Agnol et al. 2005).

Redox conditions in the Märjamaa–Kloostri system are constrained by whole-rock iron speciation (Fe^{3+}#), Fe–Ti oxide systematics, and phase-dependent differentiation. Fe^{3+} increases from Phase II through Phase I to Phase III, indicating a shift from relatively reduced to predominantly oxidized conditions (Ishihara 1977, 1981, 2004; Ishihara et al. 2000; Yang et al. 2021). In contrast, $FeO^*/(FeO^* + MgO)$ and Mg# primarily track ferroan differentiation driven by bulk Fe and Mg depletion rather than oxygen fugacity, explaining why Phase II plots in oxidized A-type fields while remaining the most reduced in terms of Fe^{3+}# (Frost et al. 2001; Ishihara 2004; Dall'Agnol and de Oliveira 2007; Yang et al. 2021). Progressive depletion of Fe–Ti oxides and accessory titanite–apatite provides independent support for this trend (Fig. 2b). Collectively, these findings suggest that FMQ-buffered conditions in Phases I and II evolve to NNO-like conditions in Phase III, indicating that redox evolution is controlled by emplacement dynamics and melt differentiation.

Evidence of magma–wall-rock interaction in the Märjamaa pluton includes gneiss xenoliths, sharp intrusive contacts, and granite apophyses cutting through the surrounding basement (Klein et al. 1994; Soesoo and Hade 2012). These xenoliths, derived from amphibolitic to tonalitic–granodioritic Proterozoic gneisses in western Estonia (Fig. 1b), provide mafic to intermediate crustal material compared to the host rapakivi magma (Soesoo and Niin 1992; Soesoo 1993; Klein et al. 1994; Kirs et al. 2004). The interaction was most pronounced during the earliest intrusive phase, Phase I, which shows the highest evidence of wall-rock interaction, with an increased presence of ferromagnesian minerals and Fe–Mg–Ti-bearing accessory phases. Phase I granites are also rich in accessory and ore minerals such as magnetite, ilmenite, and zircon, characterized by inclusion-rich, weakly zoned prismatic grains, indicative of early crystallization in a dynamic magmatic reservoir (Soesoo and Niin 1992; Klein et al. 1994).

Phase II zircons display strong internal zonation and fractures, suggesting magmatic reworking during ongoing subsidence and lateral expansion. In contrast, Phase III leucogranites contain primarily clear, weakly zoned zircons, indicating late-stage crystallization from evolved melts (Soesoo and Niin 1992; Klein et al. 1994). This shift in zircon textures corresponds to the CIPW normative trends, moving from oxide-phosphate- and calcic-rich assemblages in Phase I to feldspar-dominated, accessory-poor compositions in Phases II and III. These results show that wall-rock interaction and magmatic heterogeneity peaked during Phase I, with later phases indicating more controlled differentiation (Solano-Acosta et al. 2025b).

Whole-rock temperature proxies reveal a consistent thermal evolution across the Märjamaa–Kloostri sequence. Temperatures derived from the T_{SiO_2} formulation decrease from Phase I (~775 °C) to Phase III (~706 °C) (Table 2; Fig. 5d), consistent with the increased silica enrichment and normative quartz. T_{SiO_2} effectively tracks relative cooling during melt differentiation, while T_{MgO} yields higher, more variable estimates, reflecting sensitivity to Mg redistribution among mafic silicates, Fe–Ti oxides, and phosphate phases; it therefore represents a secondary, compositionally influenced proxy (Duan et al. 2022).

These whole-rock thermobarometric estimates are consistent with mineral-based constraints from the Märjamaa body. Amphibole chemistry and Buddington–Barth geothermometry indicate mid-crustal emplacement at 550–650 °C and 5.2–6.5 kbar (~17–22 km; Klein et al. 1994), in agreement with the Märjamaa–Kloostri emplacement model (Solano-Acosta et al. 2025b). More broadly, A-type granites are commonly emplaced at shallow- to mid-crustal levels, with magma chambers extending to ~20 km depth (Bonin 2007), along ascent paths from ~15 km (~6 kbar) under ambient crustal temperatures of 450–650 °C, while magma ascent proceeds under near-isothermal decompression and crystallization occurs at higher temperatures of ~720–780 °C (Vigneresse 2005). Emplacement depths of AMCG-rapakivi massifs typically range from 7 to 20 km (2–6 kbar), as documented for the Salmi massif (2–3 kbar; Sharkov and Bogina 2006), the Korosten pluton (3–4 kbar; Sharkov 2010), the Wiborg batholith (2.5–5.4 kbar; Elliott 2001), whose associated Suursaari quartz porphyry volcanic sequence records coeval shallow-crustal crystallization at ~1–5 kbar and ~647–738 °C (Ehrlich et al. 2012), and the Mazury Complex, which reaches zircon saturation above 840 °C at ~4 kbar (Grabarczyk et al. 2023). The Riga pluton represents the deepest end-member (5–7 kbar; 14–17 km), supported by subsolidus coronas in gabbroids formed at 5–6 kbar and 900–1100 °C (Rämö et al. 1996; Kirs et al. 2004; Sharkov et al. 2004; Sharkov 2010). In this context, the thermobarometric results indicate that the Märjamaa–Kloostri complex represents a typical mid-crustal rapakivi system consistent with Paleoproterozoic Fennoscandian AMCG magmatism.

The Märjamaa–Kloostri complex shows systematic petrophysical and mineralogical differences across three magmatic stages, reflected in CIPW normative trends and paired geochemical and geophysical signals. Phase I is a ferroan, melanocratic granodiorite rich in Fe–Ti oxides and phosphates, with high levels of normative magnetite, ilmenite, and apatite. These phases (magnetite ~5.2 g/cm^3, ilmenite ~4.7 g/cm^3, apatite ~3.1 g/cm^3) contribute to the high bulk density of Phase I ($\rho \approx 2.71$ g/cm^3) and its associated gravity and magnetic maxima (Soesoo and Niin 1992; Soesoo 1993; Klein et al. 1994; Solano-Acosta et al. 2025b). With progressive differentiation toward Phase II, dense oxide-phosphate minerals are depleted, resulting in a quartz–K-feldspar-rich assemblage with lower magnetic susceptibility and reduced bulk density ($\rho \approx 2.66$ g/cm^3). Phase III features a late, Na-rich leucogranitic melt with few oxide minerals and increased albite content, leading to the lowest bulk densities ($\rho \approx 2.59$–2.63 g/cm^3) and a strong gravity minimum. The decline in density from Phase I to Phase III indicates the removal of dense Fe–Ti oxides and Ca-rich feldspar components. Feldspar undergoes compositional changes from anorthite-rich (~2.73 g/cm^3) to orthoclase- (~2.56 g/cm^3) and albite-

dominated (~2.62 g/cm^3) assemblages. In contrast, magnetic anomalies mainly relate to magnetite distribution and shape, with local magnetic highs along the northwestern margin of Phase III caused by the superposition of the underlying Phase I magnetite-rich core or by concentrations of magnetic carriers along late-stage feeder structures active during asymmetric, trapdoor-style subsidence. Together, CIPW mineral systematics (Fig. 3) and geophysical signatures (Solano-Acosta et al. 2025b) support a multistage emplacement history involving early intrusion of a steep-sided intrusion, piston cauldron subsidence with peripheral ring emplacement, and late asymmetric intrusion during crustal relaxation.

Future research should combine whole-rock geochemistry with mineral-scale analyses to enhance our understanding of redox evolution and magma–wall-rock interactions. Specifically, evaluating whole-rock iron speciation (Fe^{3+}#), Ce anomalies, and iron isotopes in Fe–Ti oxides could shed light on oxidation mechanisms and redox timing during differentiation. Comparative studies of Estonian rapakivi bodies and the Wiborg suite in Finland, along with other Fennoscandian complexes, are essential to determine whether the observed redox signatures result from magmatic evolution, host-rock influence, or tectonic factors related to emplacement and shear zones.

7. Conclusions

Major-element systematics define a coherent, multistage differentiation sequence in the Märjamaa–Kloostri rapakivi system, evolving from a ferroan, oxide-phosphate-enriched Phase I through a strongly fractionated, K-rich Phase II to a highly evolved, quartz–feldspar–Na-dominated Phase III. This evolution is characterized by progressive silica and alkali enrichment coupled with systematic depletion of Fe–Ti–Mg–Ca-bearing and phosphate components, while Al_2O_3 contents remain broadly stable or show a slight decrease, indicating feldspar-controlled differentiation rather than variable degrees of low-pressure dehydration melting or redox-driven Al enrichment. Redox evolution is closely linked to cauldron-style emplacement dynamics: Phase I crystallized under moderately oxidized conditions with abundant Fe–Ti oxides, Phase II records the strongest fractionation but comparatively reduced conditions owing to compositional exhaustion of Fe and Ti, and Phase III represents the most oxidized yet oxide-poor stage as a consequence of advanced melt evolution. Independent thermometric estimates document progressive cooling from Phase I to Phase III, whereas thermobarometric constraints cluster within a narrow mid-crustal range, supporting differentiation within a single crustal reservoir. Together, major-element trends, normative mineralogy, and pressure–temperature constraints identify the Märjamaa–Kloostri complex as a multistage rapakivi system in which oxide abundances primarily track melt differentiation and emplacement processes, while redox variations reflect phase-specific evolutionary pathways rather than a simple, monotonic oxidation trend.

Data availability statement

Data not already included in the paper and its supplementary material will be made available upon request.

Acknowledgments

This research was partially funded by the Estonian Research Council project TemTA30 and supported by the DEXPLORE Horizon Research Funds (document No. VHE24051) through the Horizon Europe program HORIZON-CL4-2024-RESILIENCE-01-01. We also thank the EU Funding and Tenders Portal for its support, linked to project ID 101178897. We are grateful to Dr. Matti Kurhila for his evaluation and constructive review of the manuscript. The publication costs of this article were partially covered by the Estonian Academy of Sciences.

Supplementary online data

Supplementary online data to this article can be found at https://doi.org/10.3176/earth.2026.S06. The supplementary material is designed to provide complementary figures and plots enhancing the geochemical distribution patterns described in this research.

References

Ahl, M., Andersson, U. B, Lundqvist, T. and Sundblad, K. (eds). 1997. Rapakivi granites and related rocks in central Sweden. In *7th International Symposium on Rapakivi Granites, Helsinki, Finland, 24–26 July 1996*. Geological Survey of Sweden, Uppsala. https://resource.sgu.se/dokument/publikation/ca/ca87rapport/ca87-rapport.pdf

All, T., Puura, V. and Vaher, R. 2004. Orogenic structures of the Precambrian basement of Estonia as revealed from the integrated modelling of the crust. *Proceedings of the Estonian Academy of Sciences. Geology*, **53**(3), 165–189. https://doi.org/10.3176/geol.2004.3.03

All, T., Flodén, T. and Puura, V. 2006. A complex model of Mesoproterozoic sedimentary and igneous suites in a graben setting north of Gotland, Baltic Sea. *GFF*, **128**, 53–63. https://doi.org/10.1080/11035890601281053

Anderson, J. L. and Bender, E. E. 1989. Nature and origin of Proterozoic A-type granitic magmatism in the southwestern United States of America. *Lithos*, **23**(1–2), 19–52. https://doi.org/10.1016/0024-4937(89)90021-2

Anderson, J. L. and Morrison, J. 2005. Ilmenite, magnetite, and peraluminous Mesoproterozoic anorogenic granites of Laurentia and Baltica. *Lithos*, **80**(1–4), 45–60. https://doi.org/10.1016/j.lithos.2004.05.008

Andersson, U. B. and Eklund, O. 1994. Cellular plagioclase intergrowths as a result of crystal-magma mixing in the Proterozoic Åland rapakivi batholith, SW Finland. *Contributions to Mineralogy and Petrology*, **117**, 124–136. https://doi.org/10.1007/BF00286837

Barker, F. 1979. Trondhjemite: definition, environment and hypotheses of origin. In *Trondhjemites, Dacites and Related Rocks* (Barker, F., ed.). Elsevier, Amsterdam, 1–12. https://doi.org/10.1016/b978-0-444-41765-7.50006-x

Bogdanova, S., Gorbatschev, R., Grad, M., Janik, T., Guterch, A., Kozloskaya, E. et al. 2006. EUROBRIDGE: new insight into the geodynamic evolution of the East European Craton. *Geological Society, London, Memoirs*, **32**, 599–625. https://doi.org/10.1144/GSL.MEM.2006.032.01.36

Bogdanova, S., Bingen, B., Gorbatschev, R., Kheraskova, T., Kozlov, V., Puchko, V. et al. 2008. The East European Craton (Baltica) before and during the assembly of Rodinia. *Precambrian Research*, **160**(1–2), 23–45. https://doi.org/10.1016/j.precamres.2007.04.024

Bogdanova, S., Gorbatschev, R., Skridlaitė, G., Soesoo, A., Taran, L. and Kurlovich, D. 2015. Trans-Baltic Palaeoproterozoic correlations towards the reconstruction of supercontinent Columbia/Nuna. *Precambrian Research*, **259**, 5–33. https://doi.org/10.1016/j.precamres.2014.11.023

Bonin, B. 2007. A-type granites and related rocks: evolution of a concept, problems and prospects. *Lithos*, **97**(1–2), 1–29. https://doi.org/10.1016/j.lithos.2006.12.007

Buckle, T., Williams, M., Nathwani, C. L. and Hughes, H. S. R. 2023. WebNORM: a web application for calculating normative mineralogy. *Frontiers in Earth Science. Geochemistry*, **11**. https://doi.org/10.3389/feart.2023.1232256

Campbell, A. J., Danielson, L., Righter, K., Seagle, C. T., Wang, Y. and Prakapenka, V. B. 2009. High pressure effects on the iron–iron oxide and nickel–nickel oxide oxygen fugacity buffers. *Earth and Planetary Science Letters*, **286**(3–4), 556–564. https://doi.org/10.1016/j.epsl.2009.07.022

Christiansen, E. H., Haapala, I. and Hart, G. L. 2007. Are Cenozoic topaz rhyolites the erupted equivalents of Proterozoic rapakivi granites? Examples from the western United States and Finland. *Lithos*, **97**(1–2), 219–246. https://doi.org/10.1016/j.lithos.2007.01.010

Dall'Agnol, R. and de Oliveira, D. C. 2007. Oxidized, magnetite-series, rapakivi-type granites of Carajás, Brazil: implications for classification and petrogenesis of A-type granites. *Lithos*, **93**(3–4), 215–233. https://doi.org/10.1016/j.lithos.2006.03.065

Dall'Agnol, R., Rämö, O. T., de Magalhães, M. S. and Macambira, M. J. B. 1999. Petrology of the anorogenic, oxidized Jamon and Musa granites, Amazonian Craton: implications for the genesis of Proterozoic A-type granites. *Lithos*, **46**(3), 431–462. https://doi.org/10.1016/S0024-4937(98)00077-2

Dall'Agnol, R., Teixeira, N. P., Rämö, O. T., Moura, C. A.V., Macambira, M. J. B. and de Oliveira, D. C. 2005. Petrogenesis of the Paleoproterozoic rapakivi A-type granites of the Archean Carajás metallogenic province, Brazil. *Lithos*, **80**(1–4), 101–129. https://doi.org/10.1016/j.lithos.2004.03.058

Dall'Agnol, R., Frost, C. D. and Rämö, O. T. 2012. IGCP Project 510 "A-type granites and related rocks through time": project vita, results, and contribution to granite research. *Lithos*, **151**, 1–16. https://doi.org/10.1016/j.lithos.2012.08.003

Duan, M., Niu, Y., Sun, P., Chen, S., Kong, J., Li, J. et al. 2022. A simple and robust method for calculating temperatures of granitoid magmas. *Mineralogy and Petrology*, **116**, 93–103. https://doi.org/10.1007/s00710-021-00769-5

Duchesne, J.-C., Martin, H., Bagiński, B., Wiszniewska, J. and Vander Auwera, J. 2010. The origin of ferroan-potassic A-type granitoids: the case of the hornblende–biotite granite suite of the Mesoproterozoic Mazury Complex, northeastern Poland. *The Canadian Mineralogist*, **48**(4), 947–968. https://doi.org/10.3749/canmin.48.4.947

Eby, G. N. 1992. Chemical subdivision of the A-type granitoids: petrogenetic and tectonic implications. *Geology*, **20**(7), 641–644. https://doi.org/10.1130/0091-7613(1992)020<0641:CSOTAT>2.3.CO;2

Ehrlich, K., Verš, E., Kirs, J. and Soesoo, A. 2012. Using a titanium-in-quartz geothermometer for crystallization temperature estimation of the Palaeoproterozoic Suursaari quartz porphyry. *Estonian Journal of Earth Sciences*, **61**(4), 195–204. https://doi.org/10.3176/earth.2012.4.01

Eklund, O. and Shebanov, A. 1999. The origin of rapakivi texture by sub-isothermal decompression. *Precambrian Research*, **95**(1–2), 129–146. https://doi.org/10.1016/S0301-9268(98)00130-2

Eklund, O., Fröjdö, S. and Lindberg, B. 1994. Magma mixing, the petrogenetic link between anorthositic suites and rapakivi granites, Åland, SW Finland. *Mineralogy and Petrology*, **50**, 3–19. https://doi.org/10.1007/BF01160135

Elliott, B. A. 2001. Crystallization conditions of the Wiborg rapakivi batholith, SE Finland: an evaluation of amphibole and biotite mineral chemistry. *Mineralogy and Petrology*, **72**, 305–324. https://doi.org/10.1007/s007100170021.

Emslie, R. F. 1978. Anorthosite massifs, rapakivi granites, and Late Proterozoic rifting of North America. *Precambrian Research*, **7**(1), 61–98. https://doi.org/10.1016/0301-9268(78)90005-0

Frost, C. D. and Frost, B. R. 1997. Reduced rapakivi-type granites: the tholeiite connection. *Geology*, **25**(7), 647–650. https://doi.org/10.1130/0091-7613(1997)025<0647:RRT GTT>2.3.CO;2

Frost, C. D. and Frost, B. R. 2011. On ferroan (A-type) granitoids: their compositional variability and modes of origin. *Journal of Petrology*, **52**(1), 39–53. https://doi.org/10.1093/petrology/egq070

Frost, C. D., Frost, B. R., Chamberlain, K. R. and Edwards, B. R. 1999. Petrogenesis of the 1.43 Ga Sherman batholith, SE Wyoming, USA: a reduced, rapakivi-type anorogenic granite. *Journal of Petrology*, **40**(12), 1771–1802. https://doi.org/10.1093/petroj/40.12.1771

Frost, B. R., Barnes, C. G., Collins, W. J., Arculus, R. J., Ellis, D. J. and Frost, C. D. 2001. A geochemical classification for granitic rocks. *Journal of Petrology*, **42**(11), 2033–2048. https://doi.org/10.1093/petrology/42.11.2033

Gorbatschev, R. and Bogdanova, S. 1993. Frontiers in the Baltic Shield. *Precambrian Research*, **64**(1–4), 3–21. https://doi.org/10.1016/0301-9268(93)90066-B

Grabarczyk, A., Wiszniewska, J., Krzemińska, E. and Petecki, Z. 2023. A new A-type granitoid occurrence in southernmost Fennoscandia: geochemistry, age and origin of rapakivi-type quartz monzonite from the Pietkowo IG1 borehole, NE Poland. *Mineralogy and Petrology*, **117**, 1–25. https://doi.org/10.1007/s00710-022-00799-7

Haapala, I. and Rämö, O. T. 1992. Tectonic setting and origin of the Proterozoic rapakivi granites of southeastern Fennoscandia. *Earth and Environmental Science Transactions of the Royal Society of Edinburgh*, **83**(1–2), 165–171. https://doi.org/10.1017/S0263593300007859

Haapala, I., Rämö, O. T. and Frindt, S. 2005. Comparison of Proterozoic and Phanerozoic rift-related basaltic-granitic magmatism. *Lithos*, **80**(1–4), 1–32. https://doi.org/10.1016/j.lithos.2004.04.057

Heinonen, A. P., Rämö, O. T., Mänttäri, I., Johanson, B. and Alviola, R. 2010. Formation and fractionation of high-Al tholeiitic magmas in the Ahvenisto rapakivi granite–massif-type anorthosite complex, southeastern Finland. *The Canadian Mineralogist*, **48**(4), 969–990. https://doi.org/10.3749/canmin.48.4.969

Hinchey, A. M., Sandeman, H. A. and Butler, J. P. 2024. The Paleoproterozoic granite factory: voluminous post-collisional, ferroan, A-type granites and implications for crust formation and metallogenic tenor, Labrador, Canada. *GSA Bulletin*, **136**(1–2), 893–916. https://doi.org/10.1130/B36727.1

Högdahl, K., Sjöström, H. and Bergman, S. 2009. Ductile shear zones related to crustal shortening and domain boundary evolution in the central Fennoscandian Shield. *Tectonics*, **28**(1). https://doi.org/10.1029/2008TC002277

Ishihara, S. 1977. The magnetite-series and ilmenite-series granitic rocks. *Mining Geology*, **27**(145), 293–305. https://doi.org/10.11456/shigenchishitsu1951.27.293

Ishihara, S. 1981. The granitoid series and mineralization. In *Economic Geology Seventy-Fifth Anniversary Volume* (Skinner, B. J., ed.). Economic Geology Publishing Company. https://doi.org/10.5382/AV75.14

Ishihara, S. 2004. The redox state of granitoids relative to tectonic setting and earth history: the magnetite–ilmenite series 30 years later. In *The Fifth Hutton Symposium on the Origin of Granites and Related Rocks* (Ishihara, S., Stephens, W. E., Harley, S. L.,

Arima, M. and Nakajima, T., eds.). Geological Society of America. https://doi.org/10.1130/0-8137-2389-2.23

Ishihara, S., Hashimoto, M. and Machida, M. 2000. Magnetite/ilmenite–series classification and magnetic susceptibility of the Mesozoic-Cenozoic batholiths in Peru. *Resource Geology*, **50**(2), 123–129. https://doi.org/10.1111/j.1751-3928.2000.tb00062.x

Johansson, Å. 2023. A tentative model for the origin of A-type granitoids. *Minerals*, **13**(2), 236. https://doi.org/10.3390/min13020236

Johansson, Å., Waight, T., Andersen, T. and Simonsen, S. L. 2016. Geochemistry and petrogenesis of Mesoproterozoic A-type granitoids from the Danish island of Bornholm, southern Fennoscandia. *Lithos*, **244**, 94–108. https://doi.org/10.1016/j.lithos.2015.11.031

Johansson, Å., Bingen, B., Huhma, H., Waight, T., Vestergaard, R., Soesoo, A. et al. 2022. A geochronological review of magmatism along the external margin of Columbia and in the Grenville-age orogens forming the core of Rodinia. *Precambrian Research*, **371**, 106463. https://doi.org/10.1016/j.precamres.2021.106463

Kelsey, C. H. 1965. Calculation of the C.I.P.W. norm. *Mineralogical Magazine and Journal of the Mineralogical Society*, **34**(268), 276–282. https://doi.org/10.1180/minmag.1965.034.268.23

Kirs, J. and Petersell, V. 1994. Age and geochemical character of plagiomicrocline granite veins in the Abja gabro-dioritic massif. *Acta et Commentationes Universitatis Tartuensis*, **972**(14), 3–15. https://kirjandus.geoloogia.info/en/reference/3880

Kirs, J., Haapala, I. and Rämö, O. T. 2004. Anorogenic magmatic rocks in the Estonian crystalline basement. *Proceedings of the Estonian Academy of Sciences. Geology*, **53**(3), 210–225. https://doi.org/10.3176/geol.2004.3.05

Kirs, J., Puura, V., Soesoo, A., Klein, V., Konsa, M., Koppelmaa, H. et al. 2009. The crystalline basement of Estonia: rock complexes of the Palaeoproterozoic Orosirian and Statherian and Mesoproterozoic Calymmian periods, and regional correlations. *Estonian Journal of Earth Sciences*, **58**(4), 219–228. https://doi.org/10.3176/earth.2009.4.01

Kivisilla, J., Niin, M. and Koppelmaa, H. 1999. *Catalogue of Chemical Analyses of Major Elements in the Rocks of the Crystalline Basement of Estonia*. Geological Survey of Estonia, Tallinn. https://kirjandus.geoloogia.info/reference/21247

Klein, V., Konsa, M. and Niin, M. 1994. On mineralogy of the porphyraceous potassium granites of small massifs in the northern Estonian basement. *Proceedings of the Estonian Academy of Sciences. Geology*, **43**(4), 165–176. https://doi.org/10.3176/geol.1994.4.01

Korhonen, J. V., Aaro, S., All, T., Nevanlinna, H., Skilbrei, J. R., Säävuori, H. et al. 2002. *Magnetic Anomaly Map of the Fennoscandian Shield 1:2,000,000*. Geological Survey of Finland, Helsinki.

Kosunen, P. 1999. The rapakivi granite plutons of Bodom and Obbnäs, southern Finland: petrography and geochemistry. *Bulletin of the Geological Society of Finland*, **71**, 275–304. https://doi.org/10.17741/bgsf/71.2.005

Kukkonen, I. T. and Lauri, L. S. 2009. Modelling the thermal evolution of a collisional Precambrian orogen: high heat production migmatitic granites of southern Finland. *Precambrian Research*, **168**(3–4), 233–246. https://doi.org/10.1016/j.precamres.2008.10.004

Laitakari, I., Rämö, T., Suominen, V., Niin, M., Stepanov, K. and Amantov, A. 1996. Subjotnian: rapakivi granites and related rocks in the surroundings of the Gulf of Finland. *Geological Survey of Finland, Special Paper*, **21**, 59–98.

Larin, A. M. 2009. Rapakivi granites in the geological history of the Earth. Part 1, magmatic associations with rapakivi granites: age, geochemistry, and tectonic setting. *Stratigraphy and Geological Correlation*, **17**, 235–258. https://doi.org/10.1134/S0869593809030010

Le Maitre, R. W. 1976. Some problems of the projection of chemical data into mineralogical classifications. *Contributions to Mineralogy and Petrology*, **56**, 181–189. https://doi.org/10.1007/BF00399603

Le Maitre, R. W. (ed.) 2002. *Igneous Rocks: A Classification and Glossary of Terms*. 2nd ed. Cambridge University Press, Cambridge.

Loiselle, M. C. and Wones, D. R. 1979. Characteristics and origin of anorogenic granites. *Geological Society of America Abstracts with Programs*, **11**, 468.

Luo, F., Gong, H. and Liu, H. 2024. Early-Paleozoic rapakivi-textured granite from the North Qinling (Central China): implications for crust–mantle interactions in a post-collisional setting. *Mineralogy and Petrology*, **118**, 281–303. https://doi.org/10.1007/s00710-024-00861-6

Maniar, P. D. and Piccoli, P. M. 1989. Tectonic discrimination of granitoids. *GSA Bulletin*, **101**(5), 635–643. https://doi.org/10.1130/0016-7606(1989)101<0635:TDOG>2.3.CO;2

Nironen, M. 1997. The Svecofennian Orogen: a tectonic model. *Precambrian Research*, **86**(1–2), 21–44. https://doi.org/10.1016/S0301-9268(97)00039-9

Nironen, M. 2017. Guide to the geological map of Finland – Bedrock 1:1 000 000. In *Bedrock of Finland at the Scale 1:1 000 000 – Major Stratigraphic Units, Metamorphism and Tectonic Evolution* (Nironen, M., ed.). Geological Survey of Finland, Espoo, 41–76.

Nordbäck, N., Skyttä, P., Engström, J., Ovaskainen, N., Mattila, J. and Aaltonen, I. 2024. Mesoproterozoic strike-slip faulting within the Åland rapakivi batholith, southwestern Finland. *Tektonika*, **2**(1), 1–26. https://doi.org/10.55575/tektonika2024.2.1.51

Patiño Douce, A. E. 1997. Generation of metaluminous A-type granites by low-pressure melting of calc-alkaline granitoids. *Geology*, **25**(8), 743–746. https://doi.org/10.1130/0091-7613(1997)025<0743:GOMATG>2.3.CO;2

Patiño Douce, A. E. 1999. What do experiments tell us about the relative contributions of crust and mantle to the origin of granitic magmas? *Geological Society, London, Special Publications*, **168**, 55–75. https://doi.org/10.1144/gsl.sp.1999.168.01.05

Petersell, V. and Levchenkov, O. 1994. On the geological structure of the crystalline basement of the southern slope of the Baltic Shield. *Acta et Commentationes Universitatis Tartuensis*, **972**, 16–39. https://files.geocollections.info/bd4c7235-8435-49b4-8cbd-cd02e063ea92.pdf

Pirajno, F. and Santosh, M. 2015. Mantle plumes, supercontinents, intracontinental rifting and mineral systems. *Precambrian Research*, **259**, 243–261. https://doi.org/10.1016/j.precamres.2014.12.016

Puura, V. and Flodén, T. 1996. Subjotnian igneous structures in the Svecofennian domain of the Baltic region. *GFF*, **118**(S4), 22–23. https://doi.org/10.1080/11035899609546289

Puura, V. and Flodén, T. 1999. Rapakivi-granite–anorthosite magmatism – a way of thinning and stabilisation of the Svecofennian crust, Baltic Sea Basin. *Tectonophysics*, **305**(1–3), 75–92. https://doi.org/10.1016/S0040-1951(99)00019-0

Puura, V. and Flodén, T. 2000. Rapakivi-related basement structures in the Baltic Sea area; a regional approach. *GFF*, **122**(3), 257–272. https://doi.org/10.1080/11035890001223257

Puura, V., Klein, V., Koppelmaa, H. and Niin, M. 1997. Precambrian basement. In *Geology and Mineral Resources of Estonia* (Raukas, A. and Teedumäe, A., eds). Estonian Academy Publishers, Tallinn, 27–34. https://files.geocollections.info/87331eab-f8ad-423e-ac06-bcf01fa907e4.pdf

Puura, V., Hints, R., Huhma, H., Klein, V., Konsa, M., Kuldkepp, R. et al. 2004. Svecofennian metamorphic zones in the basement of Estonia. *Proceedings of the Estonian Academy of Sciences. Geology*, **53**(3), 190–209. https://doi.org/10.3176/geol.2004.3.04

Rajesh, H. M. 2000. Characterization and origin of a compositionally zoned aluminous A-type granite from South India. *Geological Magazine*, **137**(3), 291–318. https://doi.org/10. 1017/S001675680000399X

Rämö, O. T. and Haapala, I. 1995. One hundred years of rapakivi granite. *Mineralogy and Petrology*, **52**, 129–185. https://doi.org/10.1007/BF01163243

Rämö, O. T. and Haapala, I. 2005. Rapakivi granites. In *Precambrian Geology of Finland: Key to the Evolution of the Fennoscandian Shield* (Lehtinen, M., Nurmi, P. A. and Rämö, O. T., eds). Elsevier, 533–562. https://doi.org/10.1016/S0166-2635(05)80013-1

Rämö, O. T., Huhma, H. and Kirs, J. 1996. Radiogenic isotopes of the Estonian and Latvian rapakivi granite suites: new data from the concealed Precambrian of the East European Craton. *Precambrian Research*, **79**(3–4), 209–226. https://doi.org/10.1016/S0301-9268(95)00083-6

Rickwood, P. C. 1989. Boundary lines within petrologic diagrams which use oxides of major and minor elements. *Lithos*, **22**(4), 247–263. https://doi.org/10.1016/0024- 4937(89)90028-5

Salminen, J., Elming, S.-Å., Mertanen, S., Wang, C., Almqvist, B. and Moakhar, M. O. 2021. Paleomagnetic studies of rapakivi complexes in the Fennoscandian shield – implications to the origin of Proterozoic massif-type anorthosite magmatism. *Precambrian Research*, **365**, 106406. https://doi.org/10.1016/j.precamres.2021.106406

Sharkov, E. V. 2010. Middle-Proterozoic anorthosite–rapakivi granite complexes: an example of within-plate magmatism in abnormally thick crust: evidence from the East European Craton. *Precambrian Research*, **183**(4), 689–700. https://doi.org/10.1016/j.precamres.2010.08.008

Sharkov, E. V. and Bogina, M. M. 2006. Evolution of Paleoproterozoic magmatism: geology, geochemistry, and isotopic constraints. *Stratigraphy and Geological Correlation*, **14**, 345–367. https://doi.org/10.1134/S0869593806040010

Sharkov, E. V., Krassiskaya, I. S. and Chistyakov, A. V. 2004. Dispersed mafic-ultramafic intrusive magmatism in early Paleoproterozoic mobile zones of the Baltic Shield: an example of the Belomorian drusite (coronite) complex. *Petrology*, **12**(6), 561–582. https://repository.geologyscience.ru/handle/123456789/39398.

Skridlaitė, G., Whitehouse, M. and Rimša, A. 2007. Evidence for a pulse of 1.45 Ga anorthosite–mangerite–charnockite–granite (AMCG) plutonism in Lithuania: implications for the Mesoproterozoic evolution of the East European Craton. *Terra Nova*, **19**(4), 294–301. https://doi.org/10.1111/j.1365-3121.2007.00748.x

Soesoo, A. 1993. Estonian porphyraceous potassium granites: petrochemical subdivision and petrogenetical interpretation. *Proceedings of the Estonian Academy of Sciences. Geology*, **42**(3), 97–109. https://doi.org/10.3176/geol.1993.3.01

Soesoo, A. and Hade, S. 2012. Geochemistry and age of some A-type granitoid rocks of Estonia. In *Lithosphere 2012: Seventh Symposium on the Structure, Composition and Evolution of the Lithosphere in Finland, Espoo, Finland, 6–8 November 2012* (Kukkonen, I., Kosonen, E., Oinonen, K., Eklund, O., Korja, A., Korja, T. et al., eds). Institute of Seismology, Helsinki, 97–100.

Soesoo, A. and Niin, M. 1992. Petrographical and petrochemical features of the Estonian Precambrian porphyraceous potassium granites. *Proceedings of the Estonian Academy of Science. Geology*, **41**(3), 93–107. https://doi.org/10.3176/geol.1992.3.01

Soesoo, A., Puura, V., Kirs, J., Petersell, V., Niin, M. and All, T. 2004. Outlines of the Precambrian basement of Estonia. *Proceedings of the Estonian Academy of Sciences. Geology*, **53**(3), 149–164. https://doi.org/10.3176/geol.2004.3.02

Soesoo, A., Košler, J. and Kuldkepp, R. 2006. Age and geochemical constraints for partial melting of granulites in Estonia. *Mineralogy and Petrology*, **86**, 277–300. https://doi.org/10.1007/s00710-005-0110-8

Soesoo, A., Nirgi, S. and Plado, J. 2020. The evolution of the Estonian Precambrian basement: geological, geophysical and geochronological constraints. *Proceedings of the Karelian Research Centre of the Russian Academy of Sciences*, **10**(2), 18–33. https://doi.org/10.17076/geo1185

Solano-Acosta, J. D., Soesoo, A. and Hints, R. 2023. New insights of the crustal structure across Estonia using satellite potential fields derived from WGM-2012 gravity data and EMAG2v3 magnetic data. *Tectonophysics*, **846**, 229656. https://doi.org/10.1016/j.tecto.2022.229656

Solano-Acosta, J. D., Soesoo, A. and Hints, R. 2025a. Geochemistry, provenance, and tectonic setting of Paleoproterozoic metasedimentary and metavolcanic units of the Estonian Alutaguse region, eastern Fennoscandia. *Estonian Journal of Earth Sciences*, **74**(1), 61–82. https://doi.org/10.3176/earth.2025.05

Solano-Acosta, J. D., Soesoo, A. and Hints, R. 2025b. Integrated geophysical and emplacement modelling of the Märjamaa and Kloostri rapakivi granitoids, Estonia: insights into intrusion geometry and tectonic controls. *Precambrian Research*, **430**, 107938. https://doi.org/10.1016/j.precamres.2025.107938

Soosalu, H., Uski, M., Komminaho, K. and Veski, A. 2022. Recent intraplate seismicity in Estonia, East European Platform. *Seismological Research Letters*, **93**(3), 1800–1811. https://doi.org/10.1785/0220210277

Verma, S. P., Torres-Alvarado, I. S. and Velasco-Tapia, F. 2003. A revised CIPW norm. *Schweizerische Mineralogische und Petrographische Mitteilungen*, **83**, 197–216. https://doi.org/10.5169/seals-63145

Verma, S. P., Pandarinath, K., Verma, S. K. and Agrawal, S. 2013. Fifteen new discriminant-function-based multi-dimensional robust diagrams for acid rocks and their application to Precambrian rocks. *Lithos*, **168–169**, 113–123. https://doi.org/10.1016/j.lithos.2013.01.014

Verma, S. K., Torres-Sánchez, D., de León Hernández, D. A., Oliveira, E. P., Hernández-Martínez, K. R., Torres-Sánchez, S. A. et al. 2022. Petrogenesis and geodynamic implications of Oligocene A-type granite in the Guadalcazar area, San Luis Potosi, central Mexico. *Journal of Iberian Geology*, **48**, 461–486. https://doi.org/10.1007/s41513-022-00201-7

Vigneresse, J. L. 2005. The specific case of the Mid-Proterozoic rapakivi granites and associated suite within the context of the Columbia supercontinent. *Precambrian Research*, **137**(1–2), 1–34. https://doi.org/10.1016/j.precamres.2005.01.001

Whalen, J. B., Currie, K. L. and Chappell, B. W. 1987. A-type granites: geochemical characteristics, discrimination and petrogenesis. *Contributions to Mineralogy and Petrology*, **95**, 407–419. https://doi.org/10.1007/BF00402202

Yang, X.-M. 2017. Estimation of crystallization pressure of granite intrusions. *Lithos*, **286–287**, 324–329. https://doi.org/10.1016/j.939lithos.2017.06.018.940

Yang, X.-M., Lentz, D. R. and Chi, G. 2021. Ferric-ferrous iron oxide ratios: effect on crystallization pressure of granites estimated by Qtz-geobarometry. *Lithos*, **380–381**, 105920. https://doi.org/10.1016/j.lithos.2020.105920.

Ülevaade Märjamaa ja Kloostri plutooni rabakivigraniitide põhielementide geokeemiast, redokstingimustest ja petrogeneesist

Juan David Solano-Acosta, Alvar Soesoo ja Rutt Hints

Lääne-Eesti ~1,62 miljardi aasta vanused Märjamaa ja Kloostri rabakiviintrusioonid kajastavad Wiborgi kompleksse rabakiviintrusiooni hilisstaadiumi kolmeastmelist magmalist arengut. Intrusioonkehad kujunesid laialivenistuse pingete keskkonnas, mis võis olla seotud nihkevööndite reaktivatsiooniga Nuna kontinendi lagunemisel. Põhielementide geokeemiat koos CIPW normatiivsete mineraalsete faasidega kasutatakse magma evolutsiooni, redokstingimuste ja kristalliseerumismustrite hindamiseks kolmes magmalises arengufaasis. Esimene magmaline faas (I) kujundas esmase intrusioonkeha, mis arenes edasi magmakambri ülemise osa varingu ja ümbriskivimiplokkide assimilatsiooni tulemusel. I faasi kivimid varieeruvad koostiselt rauarikastest granodioriitidest kuni kvartsmonsoniitideni ning neid iseloomustab väiksem SiO_2 ja leeliste sisaldus ning suurem Ca-, Fe–Ti- ja P-sisaldus, viidates vähem diferentseerunud magmale. II faasi magma intrudeerus kontsentrilise graniitse rõngana ümber I faasi kivimi. Intrusiooni II faasi kivimid on kõige enam fraktsioneerunud, peegeldades suurt SiO_2 ja leeliste sisaldust, väikest kaltsiumisisaldust ning normatiivsete Fe–Ti oksiidide ja apatiidi väga väikest sisaldust. III faasi kivim vastab hilisele Kloostri intrusioonkehale, mis moodustus asümmeetrilise vajumise tingimustes. Tegemist on Na-rikka leukograniitse kivimiga, millel on suurim SiO_2 ja väikseim Ca-, Fe–Ti- ja P-sisaldus. Magmaline fraktsioneerumine I–III faasis väljendub süsteemsetes Fe–Mg trendides. Magma-kivimisüsteemi redokstingimused on paremini määratavad raua spetsiatsiooni alusel: II faas on redutseerunum, I faas vahepealne ja III faas oksüdeerunum. Normatiivsete Fe–Ti oksiidide vähenemine I-st III faasini peegeldab eeskätt progresseeruvat fraktsioneerumist, mitte ainult hapniku fugatsiivsuse muutusi, rõhutades põhielementidel põhinevate redokshinnangute poolkvantitatiivset olemust. Termobaromeetria viitab kristalliseerumisele keskmise maakoore tingimustes (~3–5 kbar) ja järkjärgulisele jahtumisele I-st III faasini.